RESEARCH PAPER

# THERMO-MECHANICAL REGULATION OF MATRIX DEGRADATION: COUPLED EFFECT OF PRESENCE OF CELL, APOPTOSIS AND PROLIFERATION

**Varshini P[1], Vishakha Khambhati[2]*, Dimpal Khambhati[3], Khemraj Deshmukh[4]**

[1,2,3] Department of Bio-medical Engineering, Parul Institute of Technology, Parul University, Vadodara, Gujarat, India.
[4]Department of Bio-medical Engineering, Mody University of Science and Technology, Sikar Rajasthan.

**Abstract**
The degradation of matrix that interact with cells during cellular activity is important in the area of bone tissue engineering (BTE) and regenerative medicine. This study provides numerical analysis of matrix resulting from the presence of cells, apoptosis, migration cells as a response to cryogenic temperatures. Polyelectrolyte Complex (PEC) matrix composed of porous silk fibroin will be used to assess the degradation of matrix at constant pH level or concentration 7.2. A multi-physics analysis is performed through the COMSOL Multiphysics 5.6 to assess modelling of heat transfer, solid mechanics and transport phenomena with degradation of matrix due to cryogenic temperature variations. Parameters including Temperature, Von Mises stress, Strain tensor, Displacement gradient and Deformation gradients will be characterized by matrix-cell configuration under cryogenic temperature gradients of −1, −2, and −5 K min$^{-1}$. The parallel configuration led to minimal strain $1.2 \times 10^{-3}$ and resulted in a smoother stress distribution $6.2 \times 10^7$ Pa however, there was a dramatic localization of stress with cells in the series configuration 4.8–$5.0 \times 10^7$ Pa. Additionally, in apoptosis, stress levels were measured to be high as 5.0–$5.2 \times 10^7$ Pa (-1K/min) and 7.0–$10.7 \times 10^7$ Pa (-5K/min). Although the average strain across the matrix during cell migration was measured to be $10^{-6}$, time-invariant stress created consistent migration of the cells across the entire temperature range. All effects were correlated in the numerical analysis for apoptosis, migration, and presence of cells in order to mechanistically relate the mechanics of the matrix to the behaviour of the cells and tissue regeneration.

**keywords:** Bone tissue engineering, matrix degradation, cell migration and proliferation, Apoptosis, Cryogenic effect.
**How to cite this article:** Varshini P, Khambhati V, Khambhati D, Deshmukh K. THERMO-MECHANICAL REGULATION OF MATRIX DEGRADATION: COUPLED EFFECT OF PRESENCE OF CELL, APOPTOSIS AND PROLIFERATION. Int J Drug Deliv Technol. 2026;16(8s): 815-837; DOI: 10.25258/ijddt.16.8s.92

## 1. Introduction

In bone tissue engineering, the degradation of the matrix had to be carefully coordinated with the formation of the new bone: the substance had to provide the mechanical resistance until the neo-tissue was able to support the weight, and then dissolve to allow the native matrix to occupy the space **(Zhang et al 2023; Roseti et al 2017).** Practically this balance is delicate and when exposed to extreme or non-physiological temperatures very low temperatures, cryopreservation protocols or severe sterilization and storage conditions was destabilized **(Pires et al 2016; Kehoe et al 2012)** the biomaterial and the cells within. Such conditions changed both the cell metabolism, enzyme activity, cytoskeletal mechanics and mechano-transduction and thereby reconfigured how cell sensed and remodelled the matrix which could either premature collapse or incomplete degradation of the matrix **(Gauthier and Roca-Cusachs 2023).** The degradation of matrix had continued to pose a significant impediment to bone tissue engineering and regenerative medicine globally because, it had been intrinsically challenging to scale the spatial and temporal complexity of bone regeneration with the material resorption in the case whereby the biomaterials had been subjected to extreme or non-physiological conditions during processing, storage, or implantation **(Deshmukh and Bit 2024)**. Ideally, a matrix had been able to offer transient mechanical support, direct cell adhesion and vascular proliferation, and had subsequently degraded at a pace that had been close to that of new bone formation, development, and load bearing capability **(Logeart-Avramoglou et al 2005).** In cases where the speed of degradation had been excessive, mechanical integrity of the construct was lost before adequate tissue was generated, making collapse, non-union, or fibrous repair more likely in cases where it was too slow, the matrix continued to be a foreign body, suppressed remodelling and provided stress shielding to the developing bone **(Rockwood et al 2011)**. Since achieving this synchronization was difficult, it had been opposed that matrix degradation had been reliant on a large variety of mutually dependent material and structural parameters, such as polymer or ceramic chemistry, metal corrosion behaviour, porosity, crystallinity, crosslink density and pore architecture, which also had been sensitive to manufacturing conditions **(Kehoe et al 2012).** Evaluations in general of bone tissue engineering matrix revealed that all three factors of hydrolysis, enzyme degradation and oxidation had all been shown to cause resorption and the mix of these factors had differed significantly across both synthetic polyesters, natural polymers, bioactive ceramics as well as degradable metals **(Vert et al 2012)**. As an example, the silks and other protein-based matrix had developed degradation times of between weeks and years depending on the

---

*Author for Correspondence: vishakha.khambhati12673@paruluniversity.ac.in composition of beta sheets and microstructure, whereas degradable metal matrix had been dependent on corrosion which had been highly environment dependant. This had further complicated this picture with exposure to extreme or non-physiological environment destabilizing both the matrix and cells that had been supported by the matrix. Methods of sterilization and preservation including gamma irradiation, ethylene oxide, UV exposure, and autoclaving had been critically needed in clinical practice but had also compromised molecular weight, caused chain scission, altered crystallinity and modified surface chemistry of biodegradable matrix, either rapidly accelerating, or randomly repositioning, their degradation rates **(Deshmukh and Bit, 2024).** Investigations of electro spun and porous matrix revealed that varied sterilization guidelines had elicited significant variations in mechanical characteristics and degradation patterns despite the fact that matrix geometry had not altered. Similarly, the metabolic activity, viability and cytoskeleton organisation of cells laden constructs in low temperature storage, freeze-thaw cycle and cryopreservation methods used to sustain cell laden constructs had also changed the remodelling and degradation of the surrounding matrix after thawing of cells. These environmental strains had directly acted on the cellular functions of metabolism, enzyme secretion, cytoskeletal mechanics, and mechano-transduction which had orchestrated the degradation of the matrix with matrix deposition. There had been studies of osteoblast containing cryopreservation constructs that had found a reduction in metabolic activity and disruption of actin organization after thawing which had inhibited the interaction between cells and the matrix and caused sluggish or dysregulated matrix turnover **(Bulanova et al 2020).** Combining this, the high level of processing history, sterilization and storage procedures, and local in vivo environments had ensured that matrix had hardly ever degraded in a predictable, patient specific fashion. This integration of material behaviour that is responsive to the environment, and versatile cell responses, had thus maintained matrix breakdown as among the key unresolved bottlenecks to this translational strategy of bone tissue engineering into consistency of clinical success across the globe.

Cryogenic and low temperature conditions had fundamentally repurposed biological functioning at each of the levels and thus redefined the thermomechanical responses of the biomaterial matrix on which delivered embedded or adherent cells **(Fahy et al 2004).** At the basic metabolism level, the cooling had slowed the membrane fluidity, diffusion rate and the thermal energy of biochemical reactions, all of which had reduced growth and metabolic flux in microbial and mammalian cells. To offset this, cold adapted cells were more lipid unsaturated, enhancing cold active enzymes and raising intracellular ATP and ADP pools to counter a reduction in kinetic rate, although many mammalian cells in engineered tissues had parenthetically failed to do so **(Yusof et al 2021).** Consequently, cryogenic exposure had frequently caused metabolic arrest or near complete inhibition of the oxidative phosphorylation and biosynthesis, such that after constructs were rewarmed, cells had re-entered into a mechanically active state with disrupted energy homeostasis and stress responsive signalling **(Luscombe et al., 2024).** Enzyme kinetics were also severely temperature sensitive in that, lower temperature followed Arrhenius type relationships whereby a slower rate of reaction and a change in enzyme-substrate affinity were observed. Proteases of the matrix degradation type and other enzymes that may be involved in matrix remodelling had now been demonstrated to exhibit strongly impaired activity at low temperature and essentially freeze degradation and matrix turnover during storage or cryopreservation **(Zhang et al 2023)**. These enzymes and other related reactive oxygen species pathways had already been stimulated in a microenvironment permanently altered by ice induced osmotic stress, local pH variations and microstructural damage and primed matrix to release bursts of localized activity instead of a physiological resorption profile. At the same time temperature-induced changes in membrane viscosity and protein mobility had also affected receptor clustering and signaling complexes to change still further how the cells had sensed and responded to their mechanical environment **(Stetefeld et al 2016)**. Mechanotransduction and cytoskeletal mechanics had specifically been low and cryogenic temperature sensitive. Some systems had been causing cytoskeletal arrest or partial breakdown as the actin filaments, microtubules and intermediate filaments either depolymerized or reorganized at lower temperatures (**Nilsson and Kunkel 2021**). Experiments on cryopreservation of engineered tissues had demonstrated how freezing and thawing had degraded actin architecture, cell shape and cell-matrix adhesions, unless previously particular attention had been paid to modulating cytoskeletal structures and adhesion complexes **(Xu et al 2015)**. These structural changes had modulated or warped cellular measurements of matrix stiffness, strain and topography because mechano-transduction needed intact attachments between integrins across the cytoskeleton to the nucleus and mechanosensitive ion channels. As a result, restoration of the normal integrin–FAK -MAPK and YAP/TAZ signalling pathway activated by imposed mechanical loads that would have ensured osteogenesis, matrix deposition, and survival were misrouted following cryogenic therapy **(Gauthier and Roca-Cusachs, 2023)**. These biological modifications had back-coupled with the thermos-mechanical action of the matrix themselves. In low temperature processing (as in freeze casting or cryogenic 3D printing) ice nucleation and growth had dictated pore size and orientation such that lower temperature of freezing or faster rates of freezing had grown finer and more anisotropic pore architecture with different mechanical characteristics **(Kuo et al 2020)**. It was cells which were attached to these matrices that had otherwise supported the extracellular matrix of the matrix by their cytoskeleton and adhesion complexes, and in the case of freezing had disrupted these structures, that had resulted in cell mediated strength improving the extracellular matrix **(Xu et al 2015)**. During rewarming and subsequent loading, areas of cell acquisition and loss of adhesion or apoptosis due to cryoinjury had played a less significant role in loading bearing and matrix matrixing, introducing heterogeneities in stiffness and viscoelasticity and degradation prone regions across the matrix **(Bulanova et al 2020)**. All in all, it was not simply the case that low temperature and cryogenic environment had slowed biology; it had reprogrammed metabolism, enzymatic turnover, cytoskeletal organization and mechano-transduction in the ways that had radically altered cell-matrix interactions to mechanical and thermal stimuli **(Fahy et al 2004)**. This connection had been key to the realization of why apparent structurally sound constructs on coming out of cryopreservation/cold processing had tend to show changed thermos-mechanical behaviour, non-uniform degenerative behaviour, and variable regenerative behaviour, when returned to a physiological condition.

Cell mediated responses had played the major role of driving local microenvironmental response in bone tissue engineering matrix and as such controlled locus and mode of matrix degradation **(Logeart-Avramoglou et al 2005)**. The adhesion between cells, migration, proliferation and apoptosis on the cells had maintained the biochemical milieu and mechanical landscape as stations to different spatial niches of degradation and preservation instead of a steady resorption front **(Roseti et al 2017)**. This remodelling had begun with adhesion. The actin cytoskeleton was mechanically attached to the matrix using integrin based focal adhesions, and cells were able to use them to probe ligand density and stiffness and viscoelasticity **(Discher et al 2005)**. Cytoskeletal tension and strong adherence had increased signalling axes including FAK -MAPK and RhoA - ROCK and consequently regulated expression of metalloproteinases (MMPs) and tissue inhibitors of metalloproteinases (TIMPs) and deposition of new extracellular matrix proteins **(Humphrey et al 2014)**. In areas where the matrix had matrixed a strong development of adhesion, cells had produced MMPs that had immediately softened and degraded the matrix to the localized relaxation of stress and a redistribution of how loads thereafter had been transferred. These cell mechanically active areas were commonly targets of increased cytoskeletal degradation which was accelerated, but still cell orchestrated **(Sengupta et al 2025)**. This activity had been further dispersed as migrants took part in three dimensions. By chemotactic attraction, stiffness gradient, and pore structure, cells had moved to the matrix after specific sections, as they dissipate localized ECM, MMPs, cytokine, and mineralization walls **(Chen et al 2023)**. Since the cells had invaded further into pores, or mechanically advantageous spots, they had now formed microdomains of hyper remodelling activity, with the matrix struts being gradually digested away and novels cell derived matrix being formed in its place. On the other hand, relatively undegraded in poorly populated areas had preserved original material though it also contained the possibility of mechanical mismatch with remodelled areas **(Roseti et al 2017)**. The control of the cell density and the strength of local biochemical and mechanical response, proliferation had dictated these parameters. In regions where matrix had induced high growth of mesenchymal stem cells or osteoprogenitors, there had been growth of metabolic activity, and acid, ROS, and protease production that had hastened polymer or ECM degradation and regulated mineralization forms **(Chen et al 2023)**. Meanwhile, an increasing cell layer had added new structural components cell junctions and intrinsic ECM which had modified stiffness and viscoelasticity of the composite cell-matrix construct. Recently it was demonstrated that MMP mediated matrix degradation had been found to increase stress relaxation and cells responded by modulating spreading and focal adhesion structure, strengthening a feedback loop between local degradability and mechano-transduction. Three-dimensional redistribution of this activity had been further created by migration (Logeart Avramoglou et al 2005). Under the influence of chemotactic signals, stiffness variation and pore structure, cells had moved to particular locations of the matrix, and with them local release of ECM, MMPs, cytokines and mineralization factors. The cells had already developed microdomains of high remodeling activity, with matrix struts gradually being digested away and cell derived matrix developing in their place as the cells had infiltrated deeper pores or mechanically favourable regions (Chen et al 2023). On the other hand, unpopulated areas had been in a more or less undegraded state and retained original content at the cost of facing mechanical incompatibility with refurbished areas.

Apoptosis had been spatially organized as well, in defining matrix degradation. In normal bone healing, apoptosis of osteoblast and osteoclast had been maintained in a coordinated manner with formation and resorption where one stage depended on the occurrence of the next **(Mignotte and Vayssière 1998).** Examples of osteoclast-derived apoptotic bodies had transported signaling cargos that had stimulated an osteogenic response of mesenchymal cells as well as new bone development in resorption lacunae **(Jiang et al., 2021)**. Focal apoptosis caused by mechanical loading, nutrient loss or even inflammatory stress had formed acellular spaces in matrix linked to modified pH, protease activities, and proportions of ROS, which frequently facilitated the degradation of surrounding material. The cell density and consequently the strength of local bio-chemical and mechanical reactions was predetermined by proliferation. Where matrix had stimulated the high proliferation of mesenchymal stem cells or osteoprogenators, metabolic activity and acid, reactive oxygen species and proteases production had been enhanced, which had heightened polymer or ECM degradation and controlled mineralization patterns **(Chen et al 2023)**. At the same time, a thickening cell layer had added structural elements—cell–cell junctions and endogenous ECM—that had altered stiffness and viscoelasticity of the composite cell–matrix construct **(Humphrey et al 2014)**. Recent work had shown that MMP-mediated matrix degradation had enhanced stress relaxation, and cells had responded by adjusting spreading and focal adhesion organization, thereby reinforcing a feedback loop between local degradability and mechano-transduction **(Sengupta et al 2025)** Taken together, adhesion, migration, proliferation, and apoptosis had produced self-reinforcing feedback loops (between cells and matrix) that were dynamic. The expression and matrix synthesis of MMPs had been regulated by adhesion driven mechano-transduction, migration redistribution, proliferation amplification of local biochemical and mechanical effects, and apoptosis, via clearance and apoptotic bodies, of niches and apoptotic indicators of new matrix deposition **(Humphrey et al 2014; Jiang et al 2021)**. These well-connected processes allowed cell mediated functions to remodel local stiffness, stress relaxation, porosity and biochemical makeup thus determining when and where matrix degradation had taken place in bone tissue engineering structures.

Porous matrix had previously been subjected to mechanical loading and thermally induced loading, and cellular activity had been responsive to heterogeneous degradation patters in place of uniform resorption, through mechanisms of mechano-biological feedbacks tightly coupled to both **(Hutmacher 2000)**. Combined loading of a porous structure had generated spatially heterogeneous stress and strain fields that depended upon the pore size, connectivity and stiffness gradients such that struts or small throats were strained more than large pores or sheltered areas **(Li et al 2012)**. These cells in this landscape had detected local deformation by integrins, cytoskeleton, and mechanosensitive ion channels and had altered the adhesion, cytoskeletal tension, matrix synthesis, and secretion of degradative enzymes. Since these cell-mediated changes had long-term remodelled matrix structure, there was a redistribution of stress, which supported heterogeneity in mechanical cues and matrix degradation **(Discher et al 2005)**. Location dependence Dynamic mechanical loading had typically favoured osteogenic differentiation and bone formation when geometry and stiffness of matrix had been optimally matched, although this had been highly location dependent **(Wu et al 2023)**. Continuous surfaces in well-designed porous or third wave porous matrix in a well-designed porous or triply periodic minimal surface (TPMS) matrix, dispersed loads were more organised and extreme stress concentrations were minimized and the matrix supported relatively uniform mechano-transduction and stabilized degradation **(Arabnejad et al 2024)**. Conversely, irregular or highly graded pore structures had enhanced disparities amidst the hot spots of high strain and low strain areas when subjected to the same global loading, hence neighbouring cells had undergone very dissimilar mechanical histories. Cells in high strain niches had either induced MMPS and other matrix remodelling enzymes, or had apoptosed as a result of overstrain conditions, and thus facilitated local degradation of matrix, whereas cells in mechanically protective areas had in many cases remained quiescent and had not degraded material **(Taylor et al 2025)**. This mechanically loaded matrix had been overlaid by residual stress fields which were caused by thermally induced stresses during the processing or environmental exposure **(Zhang et al 2025)**. Microcracks, densification, and pore morphology and stiffness gradient had been created in polymeric and composite materials by low temperature fabrication, freeze thaw cycling, or variable cooling. These thermally imprinted defects had been acting as stress raisers or shields when physiological loads were exerted, and this behaviour of force propagating through the matrix and cells undergoing elevated or reduced mechanical stimuli had changed. Cells in areas where thermal damage and mechanical loading had overlapped had been preferentially more prone to detach, activate stress pathways or undergo apoptosis, which released inflammatory mediators and degradative enzymes **(Fahy et al 2004)**, which had further weakened the local matrix. In other locations, the residual stress levels were lower in intact pores, and the cell behaviour was more normal and slower and controlled. The flow of fluids in the interconnected network of pores had also been regulated by mechanical loading and had also regulated movement of nutrients, oxygen and acidic or enzymatic degradation products **(Li et al 2012)**. Badly loaded and structurally blocked areas had resulted in low fluid exchange under cyclic compression and physiological loading, whereas in the regions supporting cell viability and maintaining balanced deposition and resorption flexible mechanical loading had facilitated regular accumulation of breakdown products, reducing pH and stimulating autocatalytic degradation of susceptible polymers. This was a mutual influence of load driven perfusion and local chemistry that had added to the spatially heterogeneous degradation profiles **(Hutmacher 2000)**. At cellular level, in homogeneous mechano-transduction had been a crucial mechanism which supported those patterns **(Wu et al 2020)**. Mechanically coupled tissues had been studied, which revealed that strong YAP/TAZ dependent compensatory proliferation had only been activated in cells in areas of high substrate deformation, with little being active in areas with low deformation. A similar case in porous bone matrix had led to the fact that high strain neighbourhoods were now hotspots of active remodelling and degradation, and low strain neighbourhoods had favoured retention of matrix architecture **(Arabnejad et al 2024)**. In total, mechanical loadings and thermally generated stress forces had acted on the cell mechanobiology to produce a patchwork of customized mechanical, biochemical, and cellular behaviours that had led to the heterogeneous patterns of degradation of porous matrix during bone tissue engineering **(Zhang et al 2023)**.

The current manuscript involves a numerical study of the effect of cryogenic loading, presence of cell, apoptosis of the cells, and movement of the cells on the thermo-mechanical fields and degradation behaviour of a PEC silk-fibroin matrix in bone tissue engineering. The temperature, stress, strain, and kinematic gradient will be solved at critical nodal points at different temperature gradient and matrix geometries and be synergized with simplified kinetics models and simple damage models to pinpoint possible hot spots of degradation. Finally, the research will take advantage of such findings to develop architectural principles to design cryo-treated, cell-laded matrix that have predictable and more clinical-relevant degradation characteristics.

## 2. Methodology

The aggregation of the pore domains had allowed for the creation of an interconnected transport network that enabled realistic modelling of nutrient diffusion, waste removal and heat transfer through the matrix architecture. Three different biological modelling studies (i) presence of viable cells (ii) cell apoptosis (iii) cell migration formed the basis of an established common geometry. two types of geometric configurations; serial and parallel were used to study the presence of cells and apoptosis and to evaluate how the structural arrangement of pore space affects transport and degradation characteristics. In contrast, the cell migration study utilized three different time-dependent configurations to facilitate the assessment of the temporal evolution of cell redistribution within the pore network using five distinct parameters: Deformation Gradient, Displacement Gradient, Temperature, Strain Tensor and Von Mises Stress. By applying a temperature range of 300 K to 193 K to the matrix's periphery, cryogenic temperature conditions were produced. COMSOL Multiphysics interpolation functions were utilized to create temperature gradients of -5 K/min, -2 K/min, and -1 K/min. 5.6. The matrix was in a series with the cells and media (Figures 2a), while matrix, the cells, and media were in parallel (Figure 2b). Classification of these configurations was based on relative positioning of cells in the matrix pores and cell-media interfaces. For the cell migration study, progressive shift of cell clusters from one pore to another was assumed with respect to time. The cluster of cells initially seen in pore 1 and pore 2 were indicated by $n_1$and $n_2$, respectively, whereas shifted cells from pore 1 to pore 2 were denoted by $n_3$. As indicated in Table 1, a parametric formulation was used to depict the various migration stages. This approach enabled simulation of time-dependent redistribution of cellular populations within the matrix under cryogenic conditions to 193 K. A 20 μm diameter was selected for the human endothelial cell based on published data from **(Félétou, 2011).** The silk fibroin matrix was created with PEC (later referred to as M1) which had a pore area of 0.5 mm² and was found in prior investigation provided the material properties of 1353 kg/m³ which were determined in studies **(Warwicker, 1954)**; isotropic thermal conductivity of 0.042 W/(m·K) **(Hu et al., 2007)**, and specific heat capacity is 0.478 J/(g·K) **(Pyda et al., 2008).** A previous study by **(Loh & Choong, 2013)** established that the pore diameter of both W1 (Liquid) and W2 (cytoplasm) was equal to 0.18 mm ensuring geometrical consistency between fluid and intracellular domains. W1 was completely filled with water and W2 was entirely filled with cytoplasm. The PEC-based silicone fibroin substrate is represented as a solid. It is characterized as being linear elastic and thermally conductive. The matrix has pores with a radius of 0.09 mm and measures 0.5 mm, with a porosity of approximately 68% determined by volumetric relations. Water (W1) and cytoplasmic cells (W2) were present in each of the matrix's holes. The characteristics of water were taken from the COMSOL Materials Library. The parameters for cytoplasm were provided by **(Howard et al 2019)**, which stated the following: density = 993.38 kg m$^{-3}$; thermal conductivity = 0.6252 W m$^{-1}$ K$^{-1}$; thermal expansion coefficient = 0.361 × 10$^{-3}$; and specific heat capacity = 4.178 kJ kg$^{-1}$ K$^{-1}$. As a result, there is sufficient data to accurately model thermophysical behaviour of the cytoplasm **(Deshmukh & Bit, 2024).**

**Table 1. Matrix Geometrical Parameters**

| COMPONENT | VIRTUE | UNIT | EXPLAINATION |
|---|---|---|---|
| Matrix thickness | 0.5 | mm | Reported experimental matrix dimension |
| No. of pores | 4 | - | Connected pore architecture |
| Matrix material | Silk Fibroin | - | Widely used biomaterial |
| Approximated Porosity | ~68 | % | Determined from pore-to-solid volume ratio |

**Table 2. Pore Geometrical Parameters**

| COMPONENT | VIRTUE | UNIT | EXPLAINATION |
|---|---|---|---|
| Pore Radius | 0.09 | mm | Circular pore radius |
| Pore Diameter | 0.18 | mm | Used for fluid and cytoplasm domains |
| Pore Area | 0.025 | mm² | Effective pore cross-sectional area |
| Pore Connectivity | connected | - | Allows migration and transport |

Table 1 and 2 shows the Parametric study of Matrix and pore **(Deshmukh & Bit, 2024)**

As a part of the apoptosis study, modified cellular reaction behaviour was incorporated to depict the effects of reduced metabolic activity and effects associated with releasing during apoptosis. Material properties were kept uniform for all three types of studies allowing any difference between studies to be related to the biological configurations and cryogenic temperature condition. In order to evaluate the degradation-related parameters, monitoring points P1 to P5 were established in the Matrix geometry. These five monitoring points were located so that local variations of temperature, Von mises stress, strain tensor and displacement gradient and degradation gradient also could be monitored. Points P3 and P4 were designated as P1 and P2, respectively, are the primary areas of interest for the comparative analyses since they were located and suited to represent inter-pore and matrix–cell interfaces. Under prolonged cryogenic cooling to 193 K, this approach guaranteed precise resolution of spatial heterogeneity and localized thermo-mechanical reactions.

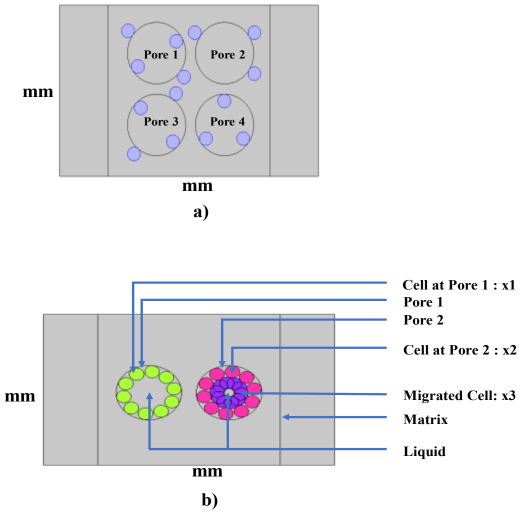

**Figure 1: (a) Placement of cell for numerical analysis of series and parallel view. (b) Schematic diagram for evaluation of matrix-cell composite for the analytical study of matrix degradation in cell migration.**

Pore 1 included both cell types located both within and exterior of the pore region. Pore 2 included only exterior to the pore region. Pore 4 contained only cells located entirely within the pore region. Although the cell designs used in pores 1 and 3 were the same, the cells' relative locations differed across these pores (Figure 1(a)). The cell and surrounding culture medium were positioned in series with the matrix in the Series View Configuration (Figure 2(a)), signifying successive mechanical and thermal coupling paths. The parallel arrangement (Figure 2(b)) had the cells and medium arranged in parallel with the matrix representing alternate conduction–convection pathways. The two configurations represented two different ways to arrange a cellular architecture; therefore, they provided an opportunity to compare their thermal and mechanical responses including stress localization and degradation behaviour. **(Deshmukh & Bit, 2024).** Figure 2 is derived from Figure 1 on the basis of cell, matrix, and liquid interaction.

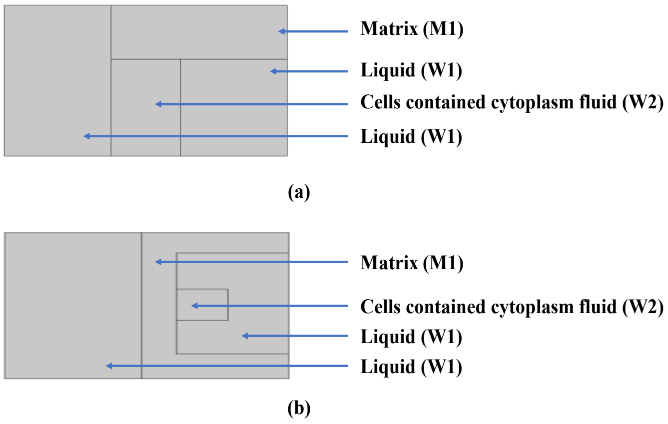

**Figure 2: Free body diagram illustrating the geometry employed for evaluation of matrix-cell composite for the analytical study of matrix degradation in presence of cell and Cell apoptosis (a). Cell- matrix interaction 1, (b) Cell- matrix interaction 2.**

In analysing cell migration, the assumption was made that as time progressed, the cell colonies migrated from pore one (1) to pore two (2) in a time-dependent manner. The initial number of cell colonies at pore one (1) and pore two (2) was referred to as n1 and n2, respectively. The number of cell colonies that migrated from pore one (1) to pore two (2) was referred to as n3. This made it possible to track how cell migration affected the silk fibroin matrix's coupled mechanical and thermal behaviours as well as the support material's deterioration. Porosity for the silk fibroin Matrix, derived from the porous structure (V) to the solid structure (Vs) ratio, was calculated using the following formula: **(Altman et al 2003; Chen et al 2024)**

$$\text{Porosity}\,\% = \langle 1 - \frac{V}{V_s} \rangle \times 100 \qquad (1)$$

According to (Kumar et al 2023), the silk fibroin matrix's porosity was calculated to be over 68%, suggesting a highly porous structure appropriate for cell migration and mass transport. A parametric investigation into the process of cell migration was undertaken to investigate the various migratory conditions outlined in Table 3. The degradation assessment closest to that of cell migration was carried out using a constant physiological pH value for each of the experiments equal to 7.2, representing a baseline physiological environment. The degradation analysis that evaluated the effect of the quantity of dye present at the cell apoptosis level (n = 0) was carried out on samples using varying levels of apoptosis: as 20% apoptosis level (6.76); 60% apoptosis level (5.88); and 100% apoptosis level (5.44). The choice of these pH values related to the expectation that increasing apoptotic activity produced progressively acidic environment, these acetification ranges are observed during late stage apoptosis and necrotic micro environments.

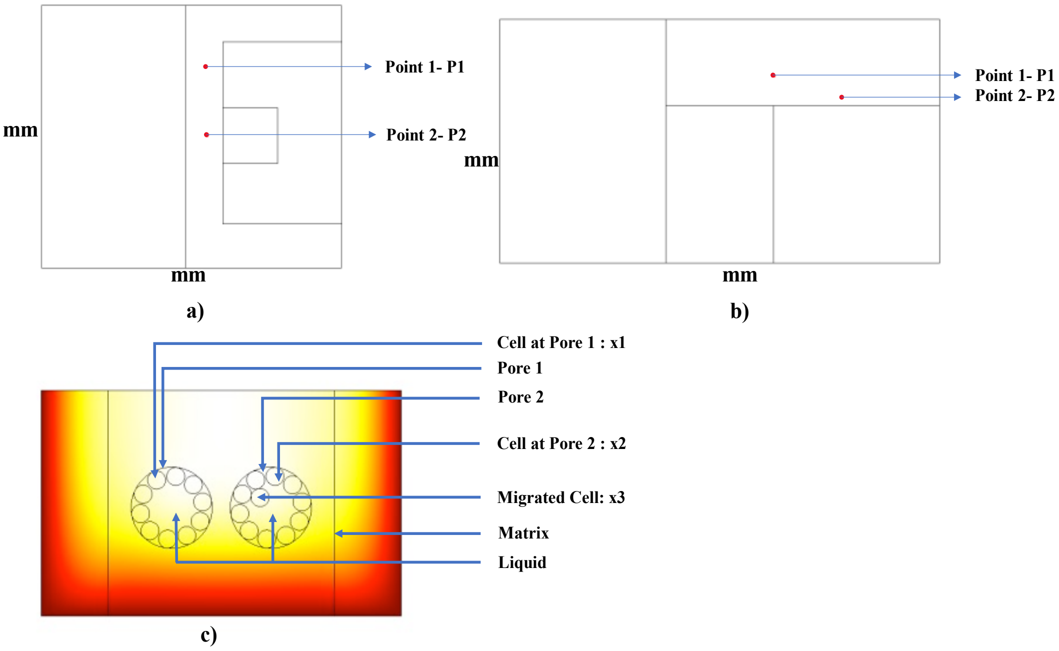

**Figure 3: Geometrical position of points P1 and P2 for evolution of parameters (a) series view, (b) parallel view, (c) schematic diagram for evolution of parameters for cell migration.**

Simulations utilizing temperature gradients of -5 K/min, -2 K/min, and -1 K/min under cryogenic temperatures 193 K (Kumar et al., 2023) investigated the effects of transitory thermal gradients on matrix degradation and mechanical behaviour. The governing equations for heat transfer in the solid and fluid components of the matrix-cell system were Fourier's Law of Heat Conduction for the solid part and Newton's Law of Convective Heat Transfer for the fluid portion, as follows: Fourier's Law of Heat Conduction illustrates the rate of heat flows through both a solid and a fluid as follows:

$$Q = \frac{kA}{L}\nabla T \qquad (2)$$

where $Q$is the heat flow rate (J/s), $A$is the surface area for heat transfer (m²), $L$is the characteristic thickness (m), $k$is the thermal conductivity (W/(m·K)), and $\nabla T$is the temperature gradient (K/m), defined the conductive heat flux formulation. For the fluid domains, Newton's law of cooling was applied:

$$Q = hA\Delta T \qquad (3)$$

where $h$ is the convective heat transfer coefficient (W/(m²·K)) and $\Delta T$is the temperature difference across surrounding surfaces and the fluid.

**Table 3. Parametric migration conditions used in the study.**

| **Condition** | **Initial Cells in Pore 1 $n_{1,\text{init}}$** | **Initial Cells in Pore 2 $n_{2,\text{init}}$** | **Migrated Cells $n_3$** | **Final Cells in Pore 1 $n_{1,\text{final}}$** | **Final Cells in Pore 2 $n_{2,\text{final}}$** |
|---|---|---|---|---|---|
| 1 | 10 | 10 | 0 | 10 | 10 |
| 2 | 10 | 10 | 3 | 7 | 13 |
| 3 | 10 | 10 | 6 | 4 | 16 |
| 4 | 10 | 10 | 9 | 1 | 19 |

$n_1$ and $n_2$ illustrates the number of cells originally present in pore 1 and pore 2, while $n_3$ denotes the number of cells migrated from pore 1 to pore 2 under each condition.

In both serially and parallelly arranged interfaces between liquids and solids there was thermal contact between solid and liquid materials in all cases. As the outcome of this direct thermal contact, the collective heat transmission was formulated using a combination of thermal resistances obtained from Fourier's law and Newton's law to predict temperature distributions across multiple material interfaces **(Bergman et al 2011)**. Therefore, these combined thermal resistance formulations allowed for accurately predicting the temperature distribution throughout the entire structure due to conduction through the solid regions and convection within the fluid region enabling multi-interface thermal resistance modelling **(COMSOL AB 2020)**. Accurate thermal-mechanical interaction was made possible by the thermal coupling of solid mechanics and transfer of heat, and temperature-dependent species transport was captured by simulating concentration distributions influenced by fluid flow, the thermal field, and the diffusion of chemical transport effects. Coupling the three physics methods simultaneously allowed for improved thermal performance of the structure and allows for the accurate simulation of the degradation process.

**Table 4. Series view, parallel view, and cell migration geometries of Mesh characteristics**

| **Parameter** | **Series View** | **Parallel View** | **Cell Migration** |
|---|---|---|---|
| Number of grid elements | 1124 | 1560 | 52,586 |
| Average mesh quality | 0.9146 | 0.9093 | 0.8306 |
| Grid area ratio | 0.4799 | 0.3135 | $4.274 \times 10^{-7}$ |
| Triangular elements | 1123 | 1670 | 52,586 |

This table shows the Parametric study for series view, parallel view, and cell migration geometries. **(Deshmukh & Bit, 2024)**

Automatic highly nonlinear was selected as the solver settings because this method is suitable with both iterative termination technique and termination technique based on tolerance. Solution convergence and residual values were both used as termination criteria for this solver. The resulting system of equations has been solved using The Multifrontal Massively Parallel Solver (MUMPS) **(Deshmukh et al. 2022)** can also solved large sparse linear systems using real and complex non-symmetric and positive definite matrices. Each column in MUMPS represented the subsequent column of the matrix that needed to be solved using a Gaussian elimination technique. Through the use of a parallel solver architecture, MUMPS was tailored for distributed memory computing settings, offering a productive way to tackle finite element problems of sizable magnitude. The finite element analysis required meshing as an integral parameter in order to accurately and reliably generate numerical predictions. Thus, how precise these numerical solutions would be became largely dependent upon how well the mesh was generated and how refined the mesh was. Specifically the characteristics of the mesh for each of these configurations (series, parallel, cell migration) were documented in Table 4. To minimize the effects of loss of heat from the system, an isotropic thermal conductivity of the material was applied to the entire computational domain. All of the geometric boundary conditions within the meshed model were initialized at room temperature enabling a laboratory environment to exist and simulated, heat flux (heat flow) applied would be treated as a uniform inward flow due to the total thermal coupling of all physical components (matrix, cytoplasm) with respect to each other being created through common mediums. The upper boundary of the matrix for both series and parallel view geometries were both treated as thermally insulated. In the solid mechanics module, the upper boundary for Figure 1(a) and the large boundary shared by fluid W1 and solid M1 in Figure 1(b) were both defined as thermally insulated enforcing adiabatic boundary conditions. Concentration influx boundaries for the transporter species are designated by the area of the upper fluid layer W2 and the small boundary that connects W2 to W1. Concentration influx boundaries for W2 in Figure 1(b) were established by excluding the connection between W2 and M2. All pore totitals and boundary layers (migrating cells) in the migration geometry have concentration parameter bounds set (Figure 2(b)). In order to simulate laboratory settings, all geometrical domains were constructed at room temperature. Heat transfer through convection through the tray into the cell, through the cell to the matrix, and through the matrix into the environment were all assumed to flow into the matrix.

### Grid Convergence Test

A major part of finite element analysis was meshing and spatial discretization. By using suitable mesh refinement techniques for all geometries, a suitable degree of mesh refinement was carried out to guarantee numerical accuracy solution convergence and computational stability. To optimize the accuracy, numerical robustness, and predictive dependability of the modelling findings, a number of factors were monitored, including mesh quality, element skewness, aspect ratio, element count, and grid area ratios.

To confirm that the numerical results were independent of mesh resolution, a grid convergence analysis was carried out. This work used the grid convergence index (GCI) approach described by **Bit and Chattopadhyay (2014)** to give formal metrics for error estimation and solution verification. Each geometry within this study (series view, parallel view, and migration) was discretized with a three different mesh density (coarse, normal, and fine). In order to define a consistent transient thermal loading condition, temperature measurements were recorded at reference point P3 for all geometries during a 23-minute simulation period with a temperature gradient of -5 K/min.

$$p = \frac{\ln\left(\frac{f_3 - f_2}{f_2 - f_1}\right)}{\ln(r)} \tag{4}$$

The grid convergence index was calculated from the mean temperature values ($f_1$, $f_2$, $f_3$) at different mesh resolutions and the refinement ratio for each of the three meshes. A logarithmic expression was utilized to define the order of convergence, and the GCI was calculated using Richardson extrapolation to predict the discretization error and truncation error boundaries based on the refinement ratios derived from the mesh spacings.

$$GCI = \frac{Fs\ lel}{(rP - 1)} \times 100\% \tag{5}$$

The observed GCI values were shown in Table 5. The mean temperature values and the GCI values confirmed that the solution was grid independent and though grid convergence was not been proven it did provide a relationship between numerical stability and the GCI values for the model.

**Table 5. Grid Convergence Index (GCI) and order of accuracy for the temperature in different geometries**

| Variable | Geometry | r | p | Fs | $GCI_{(23)}$ (%) | $GCI_{(12)}$ (%) |
|---|---|---|---|---|---|---|
| Temperature | Series view | 1.782 | 0.844 | 1.25 | 0.044 | 0.079 |
| Temperature | Parallel view | 1.744 | 2.27 | 1.25 | 0.024 | 0.112 |
| Temperature | Cell migration | 1.061 | 6.35 | 1.25 | 0.362 | 0.554 |

This table shows the Parametric study for GCI and Order of accuracy **(Deshmukh & Bit, 2024)**

### Sensitivity Analysis

A sensitivity analysis was conducted to ascertain the noteworthiness of the primary input parameters for the simulation outputs. The goal was to examine the impact of alterations in material properties **(Saltelli et al 2008)**. Using the series view of the presence of cells with temperature gradient of -5 K/min, a sensitivity analysis was performed with the following equation to represent a simplified constitutive relationship:

$$V = kT \tag{6}$$

where V is the volume of Matrix, k is the thermal conductivity of silk fibroin, and T is the temperature representing thermo-volumetric coupling behaviour. Sensitivity of volume with regards to thermal conductivity was found using the equation:

$$\frac{\Delta V}{\Delta k} = T \tag{7}$$

For the sensitivity analysis, analytical sensitivity was calculated using the temperature values at point P3 after 23 minutes representing a local sensitivity coefficient. The results of the analytical sensitivity were compared with results from the analytical sensitivity computed using two values of thermal conductivity: the original value of 6.53 W/m·K and the corresponding value with a 10% decrease, thus resulting in a thermal conductivity value of 5.85 W/m·K. The error between the analytical sensitivity and the computational sensitivity was determined to be very small (very approximately 2.65%), All geometries (defined by x = 1 to 5 in an enumeration of monitoring locations) were defined with monitoring locations (Px) and defined with other characteristics relating to degradation of cells to allow spatially resolved field evaluation. In order to evaluate the degradation characteristics of cells near pore interiors and the interfacial region of cells and matrix material, particular geometry points (P1 and P2) were chosen for parametric analysis for both series and parallel configurations. This allowed for localized interfacial assessment and micro-environmental response analysis.

## 3. Result

Cellular matrix degradation is an important process that needs to be evaluated since it provides essential information about the interaction between the cellular environment and the matrix. The evaluation helps determine the biocompatibility of the matrix, its ability to promote cellular and the most desirable rate of degradation to guarantee proper tissue remodelling and incorporation. In the presence of cells, matrix degradation was evaluated for both series (Figure 4a–4e) and parallel (Figure 5a–5e) configurations by monitoring temperature, von Mises stress, strain tensor, displacement gradient and deformation gradient at nodal points P1 and P2 for different temperature gradients. This had allowed identification of the critical temperature gradients and nodal locations governing the onset and progression of degradation in the cell-seeded matrix.

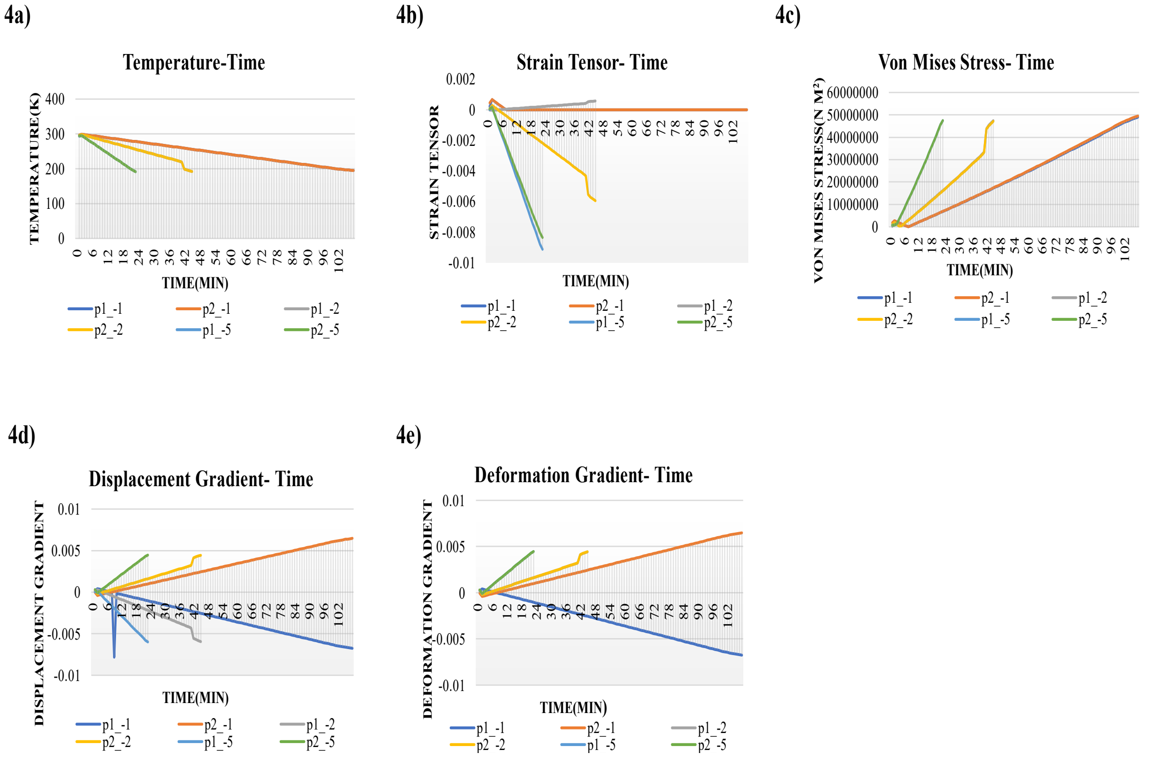

**Figure 4: Distribution of various parameters in the presence of cells for series view: 4a) Temperature vs. time, 4b) Von Mises stress vs. time, 4c) strain tensor vs. time, 4d) displacement gradient vs. time, and 4e) deformation gradient vs. time for different temperature gradients (−1, −2, and −5 K/min) at representative nodal points**

In both cases, the temperature dropped gradually from around 293K to nearly 255K, but the higher cooling rate was observed at larger gradients. Viewed as a series, P2 achieved a temperature of 260K at 8 minutes—slightly sooner than P1 which reached 255 K at 9 minutes. P1 also exhibited a larger drop from 286K (7 min) to 260K (8 min) and finally 255K (9 min) than any other combination of monitored scenarios to reach cryogenic temperatures; thus, P1 was the first to achieve the cryogenic temperature from a series configuration. Von Mises stresses (Figures .4c and 5c) demonstrated a distinct correlation to both the position of the node and its temperature gradient. In the series configuration, the greatest amount of von Mises stress occurred at P1 temperature of −2 K/min (from 3.00 × $10^6$ N/m² on 7 min. to approximately 1.74 × $10^7$ N/ m² at 10 min.); however, due to lower values for P2 at this same temperature the peak stress for the series configuration occurred at P1 under −2 K/min . The beginning of the von Mises stress had a baseline for both parallel configurations at P1 and P2 similar to what was observed for the series configuration at P1; therefore, the parallel conversions also demonstrated an increase in von Mises stress to approximately 1.67 × $10^7$ N/m² (P2) to approximately 1.66 × $10^7$ N/m² (P1) at each point in time from their respective baseline.

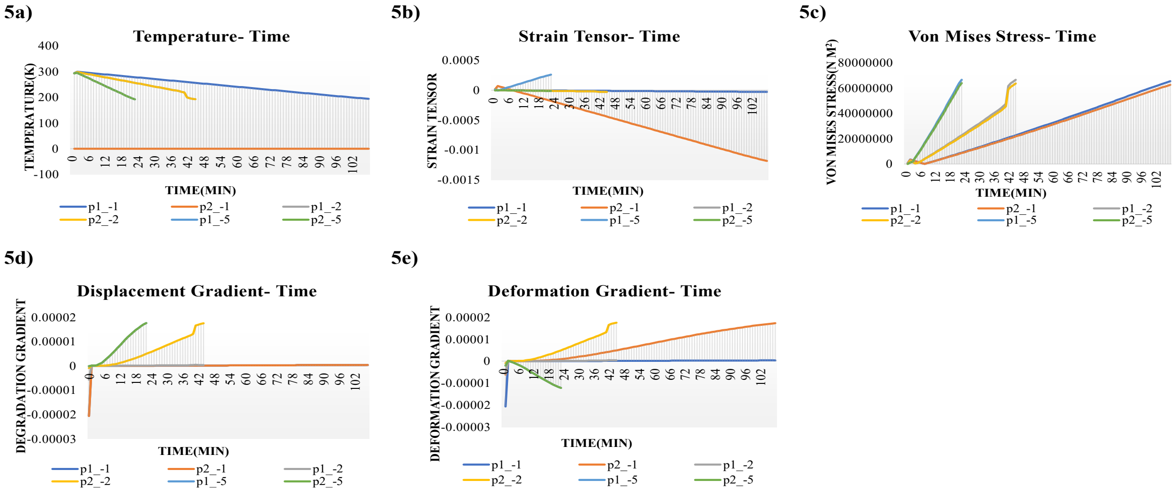

**Figure 5. Distribution of various parameters in the presence of cells parallel view: 5a) Temperature w.r.t. time, 5b) Strain tensor w.r.t time, 5c) Von Mises stress w.r.t time, 5d) Displacement gradient w.r.t time, and 5e) Deformation gradient w.r.t time for temperature gradients of −1, −2, and −5 K min⁻¹**

According to the deformation programme and the strain tensor measurements (Figs 4(b) & 5(b)), measurements indicated the region where maximum deformation had developed. When comparing the change in strain at P1 and P2 for −2 K $\text{min}^{-1}$ in the series orientation, the total change in strain experienced by P1 was from $4.05 \times 10^{-5}$ at 7 min to a maximum compressive strain of $-3.42 \times 10^{-3}$ at 9 min. At P2, the change was from $-4.17 \times 10^{-4}$ at 7 min to a maximum of $-3.13 \times 10^{-3}$ at 9 min which indicates that the maximum compressive strain for the −2 K $\text{min}^{-1}$ gradient occurred between 8 and 9 min for P1 & P2 in the series orientation. Analysis of the parallel strain data indicated that a similar amount of compressive strain (order of $10^{-3}$) was observed at P1 and P2 at the end of cooling for the −2 K $\text{min}^{-1}$ gradient and, as such, the maximum compressive strain observed at the nodes associated with the −2 K $\text{min}^{-1}$ gradient was distributed evenly as compared with the P1 & P2 in their respective orientations. The displacements and deformation gradients (Figures. 4(d)–4(e) & 5(d)–5(e)) were used to clarify the kinematics of degradation. At P1, the displacement gradient for -2 K/min had progressed from -1.02 x $10^5$ at 7 min to a maximum of -2.24 x $10^4$ at the end of cooling for the -2 K/min cooling rate at 10 mins. At P2, prior P2 had changed from 9.77 x $10^6$ to 1.40 x $10^4$ after 9 mins and also to 1.94 x $10^4$ at 10 mins and thus, indicates that P1 was the site of maximum contraction at the -2 K/min cooling rate and P2 was posturing transient stretch prior to contracting. The deformation gradient curves remained at the same relative level ($10^4$) and with maximum at the end of cooling -2 K/min, indicating that the deformation gradient was primarily responsible for local kinematic changes in the series configuration versus that at P2 in the parallel configuration. In the parallel configuration, the deformation gradient and displacement gradients at both P1 and P2 remained between $10^5$-$10^4$ with no sharp peaks in these series for all observations, thus, the magnitude of maximum kinematic gradients were smaller and less localised at P1 than were the gradients at P2 in the series configuration for the -2 K/min cooling rate. Of these graphs (Figures 4a-4e and 5a-5e) show that for both parallel and serial configurations, P1 in a serial configuration is subjected to the largest amount of stress/deformation -2 K/min while both P1 and P2 have the same amount of stress when in a parallel configuration. Serial configurations experienced high levels of stress with steep gradients, suggesting local degradation at the cell–matrix interface, whereas both P1 and P2 experienced similar amounts of stress with smoother gradients, suggesting a more evenly distributed but still intense level of local degradation at the cell-matrix interface.

Cell apoptosis may have an adverse effect on the degradation of the matrix since progressive cell death have increased the biochemical environment and the thermo-mechanical response of the PEC-silk fibroin matrix. The graph shows the temperature, von Mises stress, Strain tensor, Displacement gradient, and Deformation gradient, in bottom to top order of the apoptosis about 20%, 60%, and 100%, in both parallel and series configuration displays all of the node points and gradients from which the Max or Min values were measured. The graphs of temperature versus time, display the temperature profiles have not changed significantly for parallel and series configuration at each level of apoptosis. The temperature profiles show that the temperature has almost linearly decreased from the starting temperature of 293K to the cryogenic temperature of approximately 195K after 23 minutes of time. The lowest recorded temperature in the parallel configuration was -1 K $\text{min}^{-1}$ at the temperature of

193.95 K after 100 minutes at node point P2; At node point P2, the lowest recorded temperature in the parallel arrangement was -1 K/min at a temperature of 193.95 K after 100 minutes, and the lowest recorded temperature in the series setup was approximately 191.44 K at both P1 and P2; thus, while cell apoptosis had no effect on final temperature, it does mean that P2 had the lowest temperature of all points in the parallel arrangement.

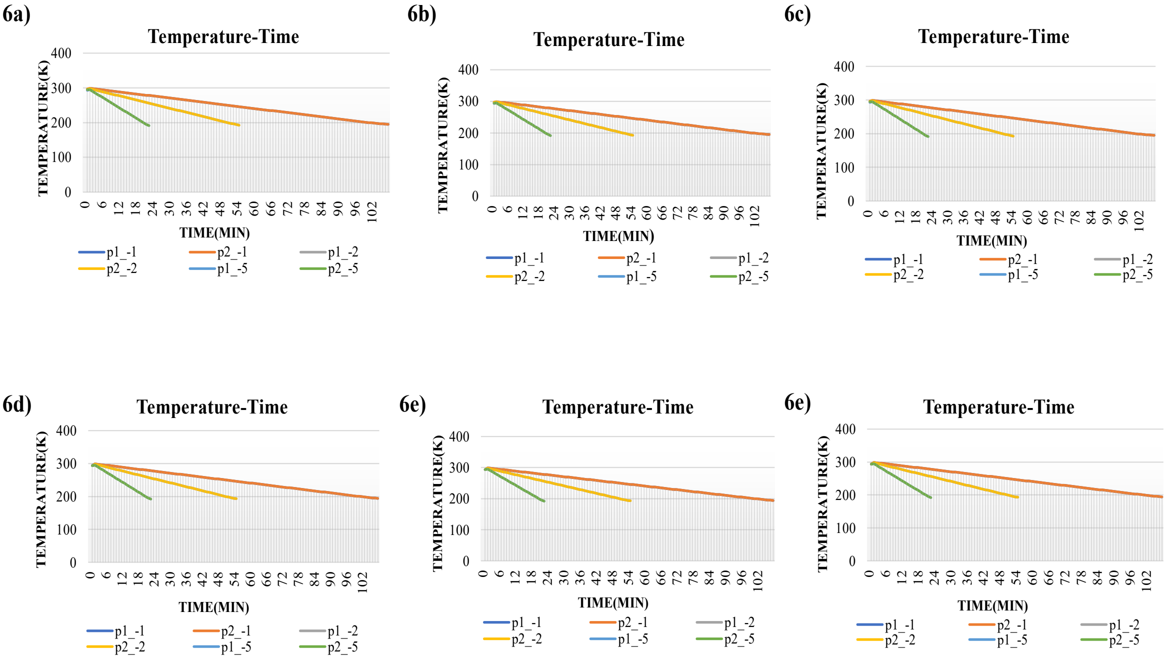

**Figure 6: Distribution of various parameters in cell apoptosis in series and parallel view; 6a) Temperature w.r.t Time at 20%, 6b) Temperature w.r.t time at 60 %, 6c) Temperature w.r.t time at 100%, 6d) Temperature w.r.t Time at 20%, 6e) Temperature w.r.t time at 60 %, 6f) Temperature w.r.t time at 100%**

The strain tensors shown in Figures 7a to 7f exhibit the same trend of being similarly positioned at a rate of -2 K min -1 (100% apoptosis) for all nodes within the series view. The highest and lowest (most negative) compressive strain from series view is -1.2 × 10 -3 at P1 at 60 min and - 1.18 × 10 -3 at P1 at a rate of -1 K min -1 at 100 min. The extent of compressive strain at P2 for a rate of -5 K min -1 at the period of time of 60 minutes is -1.23 × 10 -3 respectively. For series view, the maximum value of compressive strain was noted to be -3.40 × 10 -3 at P1, while the lowest value of compressive strain recorded was of -1.00 × 10 -3 at P2 with a total of 20% of the cells undergoing apoptosis. When testing under parallel configuration, P1 at -2 K min -1 has achieved compressive strain values in the order of 1.44 × 10 -5 when 100% of the total cells underwent apoptosis. When testing at 20% of the total cells undergo apoptosis, the compressive strain recorded is closer to -1.00 × 10 -3. These findings provide support for the premise that parallel configuration has demonstrated similar maximum values of the total compressive strain when comparing nodes within the respective configuration. Hence, apoptosis does not appear to substantively affect the compressive strain pattern but rather only the overall magnitude of the compressive strain at parallel P1 will be greater than any of the other configurations.

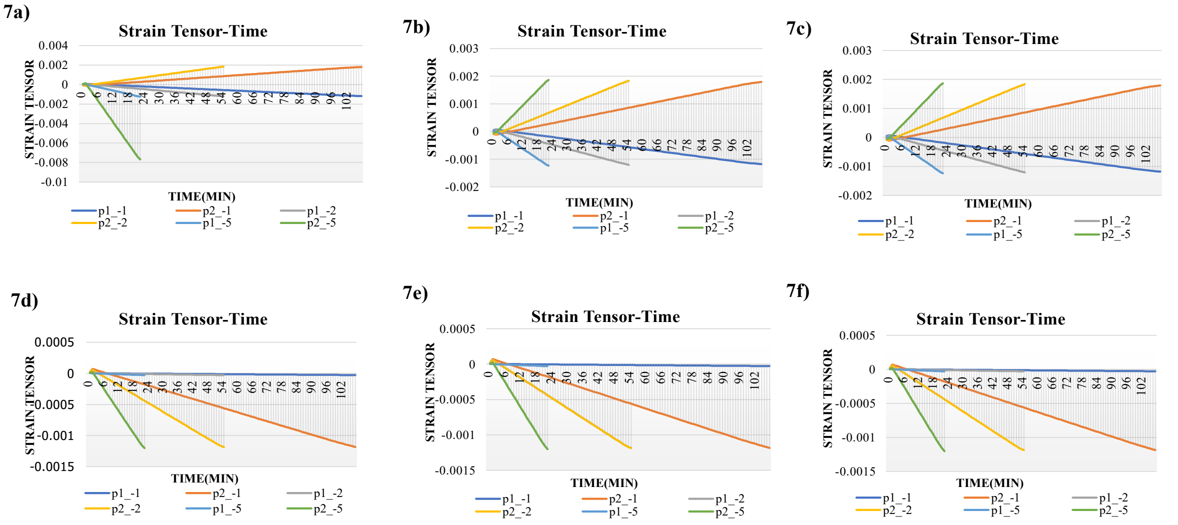

**Figure 7: Distribution of various parameters in cell apoptosis in series and parallel view 7a) Strain Tensor w.r.t time at 20%, 7b) Strain Tensor w.r.t time at 60%, 7c) Strain Tensor w.r.t time at 100%, 7d) Strain Tensor w.r.t time at 20%, 7e) Strain Tensor w.r.t time at 60%, 7f) Strain Tensor w.r.t time at 100%**

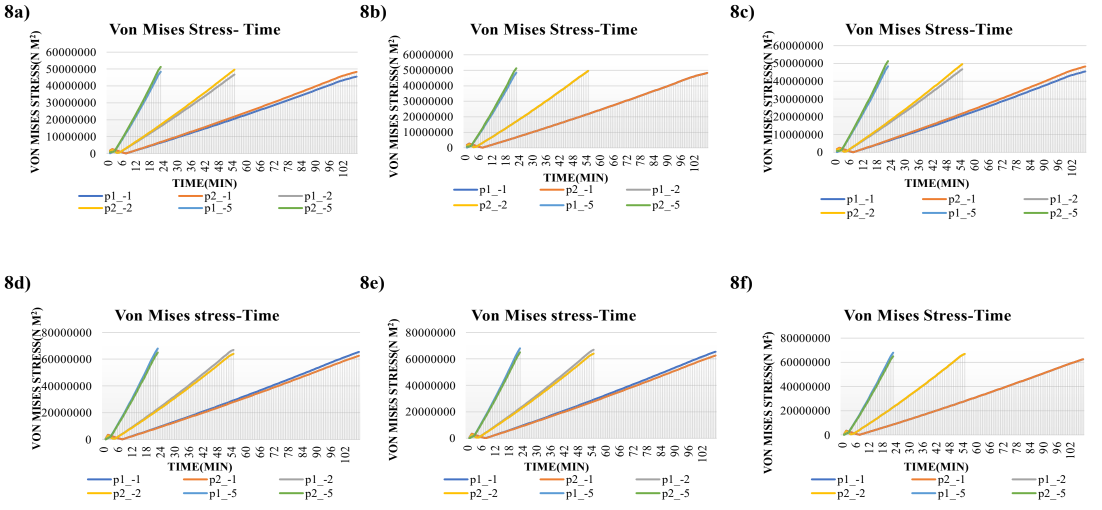

**Figure 8: Distribution of various parameters in cell apoptosis in series and parallel view: 8a) Von Mises Stress w.r.t time at 20%, 8b) Von Mises Stress w.r.t time at 60%, 8c) Von Mises Stress w.r.t time at 100%, 8d) Von Mises Stress w.r.t time at 20%, 8e) Von Mises Stress w.r.t time at 60%, 8f) Von Mises Stress w.r.t time at 100%.**

As with the base paper, von Mises stress (Figures 8a-8f) did exhibit a clear dependence on gradient and geometry. An example of this can be seen in the series configuration where the P1 stresses for the −2 K min$^{-1}$/100% apoptosis condition; approximately 1.2 × 10$^{6}$ N m$^{-2}$ at 49 min and peaked at 6.64 × 10$^{7}$ N m$^{-2}$ at 100 min. As for the P2 condition, this node reached a slightly lower peak of approximately 6.8 × 10$^{7}$ N m$^{-2}$, thus indicating that P1 had attained the peak stress condition at −2 K min$^{-1}$/100% apoptosis in the series configuration. In the parallel case, the stress values at both P1 and P2 were significantly greater; P1 and P2 both started out from a baseline around 1.2 × 10$^{7}$ N m$^{-2}$ at 20 min, peaked at 7 × 10$^{7}$ N m$^{-2}$ at 100 min (as with the series configuration), and appear nearly symmetrical in peak stress but differed in the amount of time spent at or near peak stress (i.e., long duration for parallel vs. short duration for series). Therefore, for all gradients, the maximum stress distributions were much more pronounced and evenly spread out in the parallel configuration relative to those observed in the series configuration.

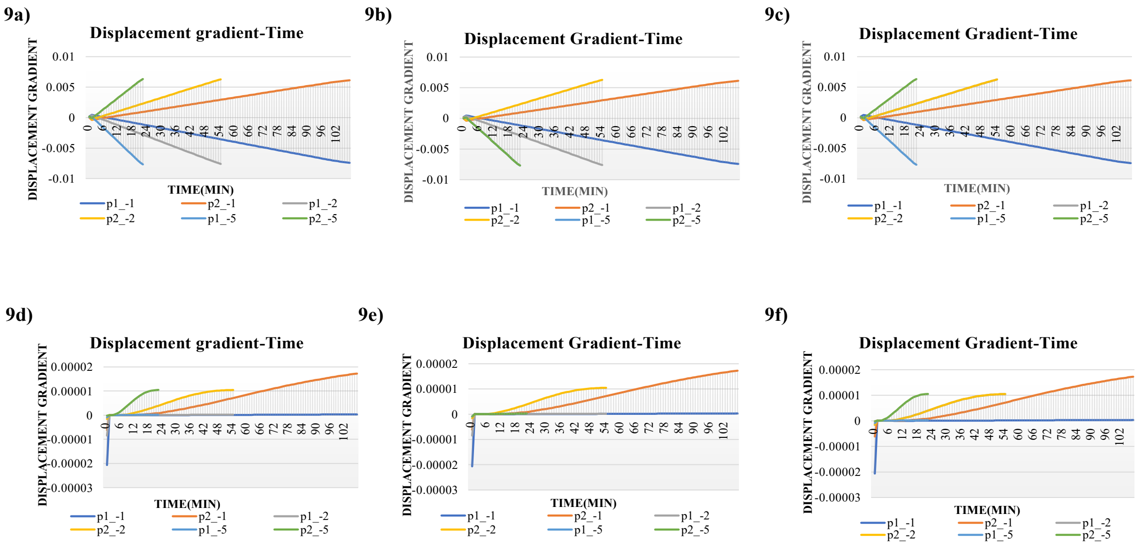

**Figure 9: Distribution of various parameters in cell apoptosis in series and parallel view: 9a) Displacement Gradient w.r.t time at 20%, 9b) Displacement Gradient w.r.t time at 60%, 9c) Displacement Gradient w.r.t time at 100%, 9d) Displacement Gradient w.r.t time at 20%, 9e) Displacement Gradient w.r.t time at 60%, 9f) Displacement Gradient w.r.t time at 100%.**

At P1(Figure 9c) under −2 K min$^{-1}$ at 100% apoptosis, the displacement gradient in series view had advanced from -1.02 × 10$^{-5}$ after 60 minutes to a lowest value of -2.24 × 10$^{-4}$ after 100 minutes, while at P2 it progressed from 9.77 × 10$^{-6}$ to 1.40 × 10$^{-4}$ after 90 minutes and then to -1.94 × 10$^{-4}$ after 100 minutes; thus, the maximum negative gradient of P1 in series had corresponded with the strongest contraction and P2 had experienced a transient positive peak. The deformation gradient curves, after about 5 minutes, also presented appreciable curvature similar to the reference description, and during all stages of apoptosis (all levels of apoptosis) the displacement and deformation gradients at P1 and P2 maintained approximately the same curvature shape within the range of -3.00 × 10$^{-5}$ to 2.00 × 10$^{-4}$ with outlier peaks in parallel view at each 0 min interval for each level of apoptosis and therefore have smaller gradients than in series (with the largest positive gradient of approximately 2.00 × 10$^{-4}$ at P2 at -2 K min$^{-1}$ at 100% apoptosis) and the smallest negative gradient of approximately -3.00 × 10$^{-4}$ at P1.

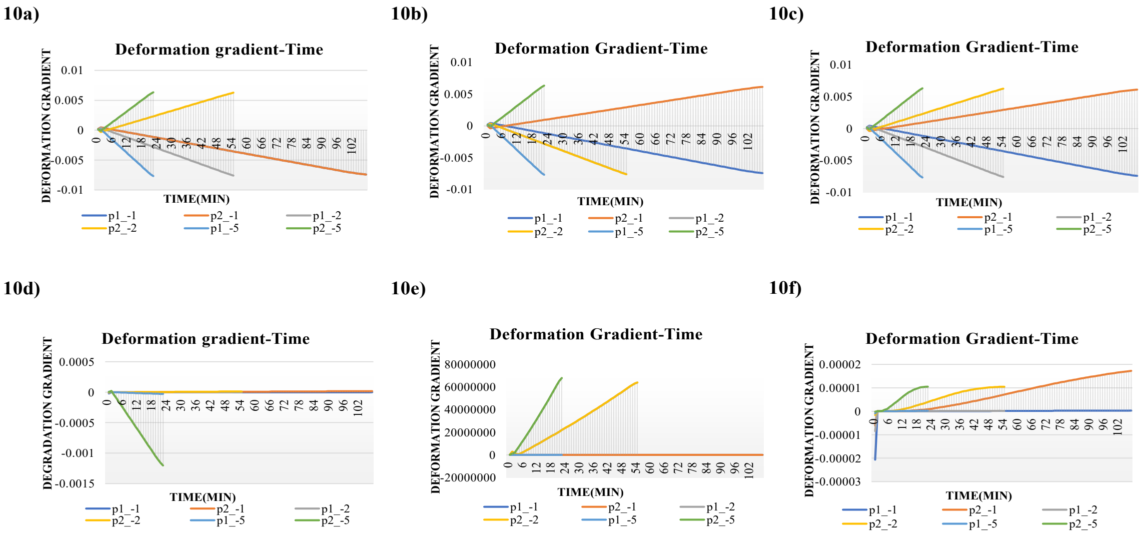

**Figure 10: Distribution of different parameters in cell apoptosis in series and parallel view: 10a) Displacement Gradient w.r.t time at 20%, 10b) Displacement Gradient w.r.t time at 60%, 10c) Displacement Gradient w.r.t time at 100%, 10d) Displacement Gradient w.r.t time at 20%, 10e) Displacement Gradient w.r.t time at 60%, 10f) Displacement Gradient w.r.t time at 100%.**

Thermal histories for all three geometries were quite similar as far as the thermal histories were concerned, although the peaks and valleys of each geometry were different. The extreme values for P1 in a series orientation were −2 K min$^{-1}$ with a Longitudinal Mechanical Stress Value of approximately 7.00 x 10$^{7}$ N/m$^{2}$ at maximum compressive strain of approximately = -3.40 x 10$^{-3}$ and maximum negative mechanical gradient of approximately 2.24 x 10$^{4}$ or P2 has rounded up to −1 K min$^{-1}$ with a total power applied to the structure measured in terms of a mechanical loading rate measured in accordance with K = 1.92 x 10$^{2}$. In addition, due to their respective geometries, both P1 and P2 exhibited nearly the same peak mechanical loads at the three different degrees of change from the zero position, but P1 and P2 had different mechanical gradients due to their different deformation patterns.

When cells migrate through an ECM, they come into contact with the ECM that is in the proximity of the migrating cells. As a result of this contact, the ECM will deform and the mechanical properties of the ECM will also change. As a result of the deformation of the ECM at the molecular level, the ECM will experience a change in the mechanical properties of the ECM. The data indicates that all of the parametric distributions of the temperature gradients resulted in a spatially uniform temperature distribution of (193 K) at all of the geometric locations of the porous matrix (figure. 11a)

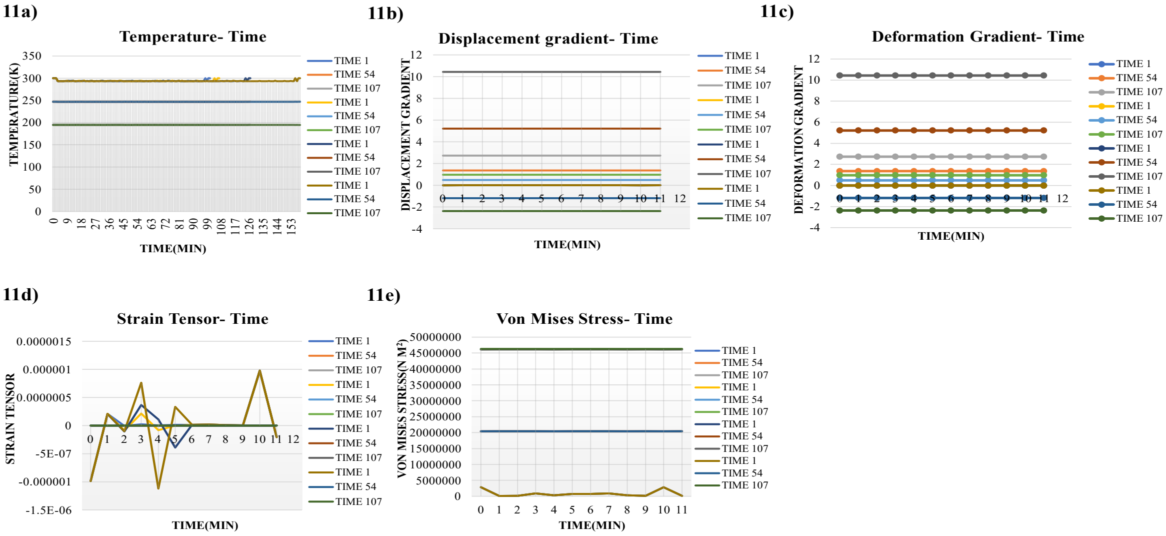

**Figure 11: Temporal evolution of 11a) temperature w.r.t time, 11b) displacement gradient w.r.t time, 11c) deformation gradient w.r.t time, 11d) strain tensor w.r.t time, and 11e) von Mises stress w.r.t time during cell migration under (−1K/min) condition.**

The upper region maintained 300 K, the intermediate region was 250 K, and the lower region around 195 K. The fact that there was no change in time shows that there was no growth in the thermal gradient applied during migration and was indicative of a thermally balanced environment where cellular migration occurred. It can be noted that the displacement response to the gradient (Figure.11b) was independent of time in each of the three regions. The displacement of each positive and negative gradient of displacement, when assessed over time, did not demonstrate any systematic change. It was shown, then, that at no point during cell migration did cumulative translational matrix deformation occur, affecting cell migration. Figure. 11d were of a very small order (in the neighbourhood of 10$^{-6}$), with slight periodic oscillations of individual steps in time. There was no variation in the von mise stress distribution (Figure. 11e) throughout the duration of the simulation, indicating that the von mises stress levels of 4.6 × 10$^{7}$ Pa, 2.0 × 10$^{7}$ Pa and near zero were either not exceeded during the duration of migration or there was no progression or change in stress levels. Overall, both Fig. 11a and Fig. 11e indicate that cellular migration at −1 K min$^{-1}$ took place under a mechanically neutral environment, where there was no irreversible deformation or strain accumulation and cellular migration occurred without the use of mechanical stability of the matrix.

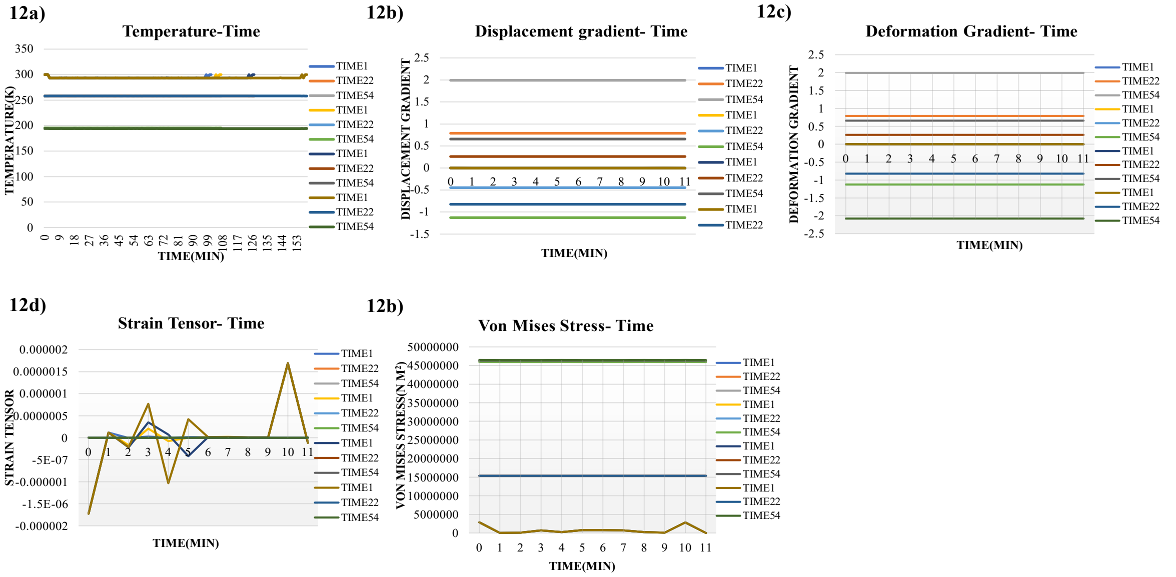

**Figure 12: Temporal evolution of 12a) temperature w.r.t time, 12b) displacement gradient w.r.t time, 12c) deformation gradient w.r.t time, 12d) strain tensor w.r.t time, and 12e) von Mises stress w.r.t time during cell migration under (−2K/min) condition.**

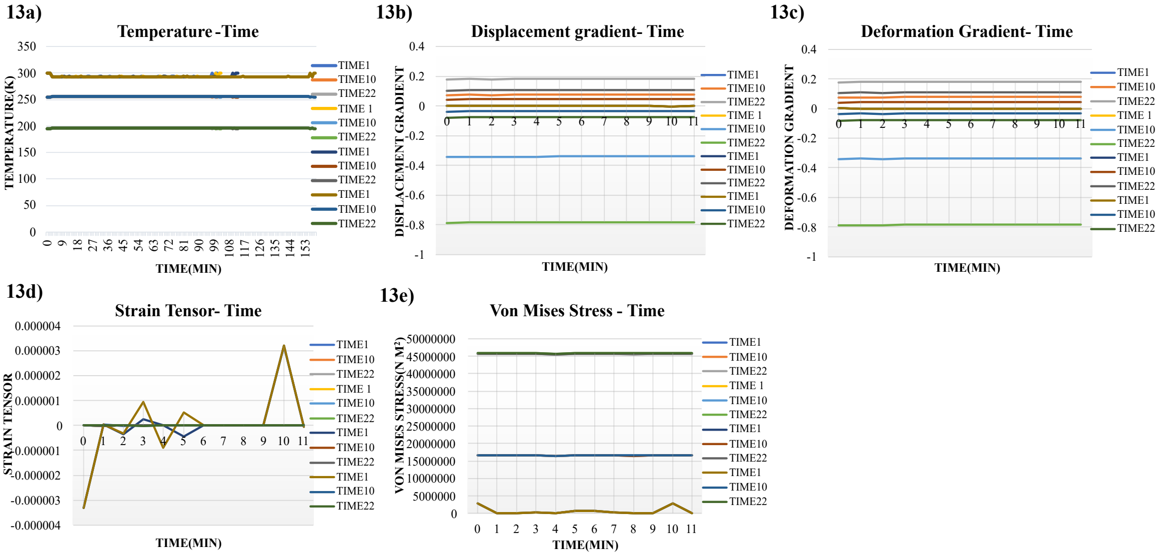

**Figure 13: Temporal evolution of 13a) temperature w.r.t time, 13b) displacement gradient w.r.t time, 13c) deformation gradient w.r.t time, 13d) strain tensor w.r.t time, and 13e) von Mises stress w.r.t time during cell migration under (−5K/min) condition**

The behaviour of cell migration process was measured using thermal and mechanical parameters measured over time ( Figure. 12a-e), during which the behaviour of cells migrating at -2 K per minute was examined together with the temperature and stiffness trends over time, the method of determining displacement gradients, measuring the straining valuue and finally measuring von Mises stress at various intervals throughout the experiment (Figure.13e). Essentially, no significant differences in temperature curves were observed, with range of -2 or +2 from a value of -1.2 to +1.2 indicating consistency of thermal support with respect to thermal/movement stability; the observed presence of negative and positive displacement values (maximum of approximately $-10^{-6}$) indicate that zero strain was produced, and the overall activation state of thermally induced mechanical behaviour of the cellular material is in the elastic regime due to the low level of maximum von Mises stress of either $1.5 \times 10^7$ or $4.6 \times 10^7$ Pa throughout the duration of the experimental run, with only sporadic maximum thickness values being achieved, near the beginning (t=0) or end (t=12) of the experimental run. Therefore, it may be concluded that at temperatures longer than -2 K/min, the thermal/mechanical conditions under which the cellular movement occurred are consistent with respect to the respective levels of thermal/mechanical support distributed over the region occupied by the cellular entities.

The temperature time profile at -5K/min (Figure 13a) was spatially homogeneous, and also time-independent during the entire simulation, and three distinct thermal plateaus were found at around 295K, 300 K, 255 K and 195 K. The lack of time-dependence confirmed that there were no thermal fluctuation and migration-related processes. The displacement gradient (Figure 13b) was found to behave time- independently at all the observed sites. The values of both positive and negative displacement gradients had not been large enough to exceed the very narrow limits, having reached only maximum values of approximately 0.15–0.18 and minimum values of approximately −0.75. The same pattern had been observed in the deformation gradient which had not changed significantly over the time except that the range had remained between about -0.8 and +0.15 indicating that local deformation of the matrices stabilized quickly and did not expand to large magnitude. Figure 13d of the strain tensor revealed very small values, most of which had been the order of $10^{-6}$ and transient oscillations at early and late times. Von Mises stress distribution (Figure13e) remained almost stable over the course of the simulation and the primary levels of stress were also at about $4.6 \times 10^7$ Pa and $1.5 \times 10^7$ Pa and only short low-frequency fluctuations having appeared at the start and the end of the time cycle. Altogether, Figure 13a–13e had shown that cellular migration occurred in thermo-mechanically stable conditions, where the displacement was steady, the strain was localized minimally, and the stress remained controlled, which proved the fact that the matrix safely supported migratory cellular activity without becoming structurally unstable.

## 4. Discussion

The need to treat cellular matrix degradation as a key finding had been critical given that it had been known to the interaction, and to be relegated by the surrounding cellular environment, as opposed to acting as a passive support in the case of the PEC silk fibroin matrix **(Kopp et al 2019)**. The analysis had been pre-empted by other reports that had concluded that both biocompatibility and the rate by which degradation could allow cell adhesion **(Nair et al 2007)** and migration followed by, but was not limited to, tissue ingrowth and vascularisation had been essential in the success or failure of tissue engineering constructs. The temperature, von Mises stress, strain tensor, and displacement gradient and deformation gradient at P1 and P2 also made the case of series and parallel configuration to examine the multi-physics window of how the combination of cryogenic loading, matrix topology and cell presence had jointly contributed to define the local degradation landscape. The nodal, gradient based methodology had permitted identification of those combinations of cooling rate and position where thermo-mechanical “hot spots” had developed and these are normally linked to increased enzymatic attack rate, pH changes and oxidative damage in cell laden degradable matrices. Consequently, the simulations had not only measured the initiation of degradation but also told which temperature gradients and nodal positions had controlled the initiation and progression of the loss of the matrix in the cell seeded PEC matrix, which provided mechanistic information on how to modify future cryogenic conditions and matrices to form. The temperature profiles in series and parallel configurations had suggested that stabilized and spatially coherent cooling of the PEC silk fibroin matrix **(Ataol 2014)** had occurred due to cryogenic protocol, and not due to localized thermal shocks. This gradual decay between 293K and the cryogenic values of a few hundred kelvins with only minor variations in the duration of time required to get specific nodes into the desired range had indicated a well-controlled heat removal and was not due to numerical artefacts or suppression. The node had been more coupled to the cooling boundary which at P2 in the series view and P1 in parallel view were slightly earlier drops had suggested that at these nodes first would be seen any temperature dependent changes in cell activity and the stiffness of the matrices, i.e., reduced enzymatic degradation or altered secretion of MMPs **(Zhang and King 2020)**, when subjected to a reduced level of K $\min^{-1}$. The monotonous behaviour of the temperature vs. time curves confirms heat transfer in the matrix–cell system, and the absence of sudden temperature fluctuations or numerical instabilities supports that the equations governing heat transfer were implemented properly, in addition to the fact that mesh resolution and solver parameters were sufficient to obtain the transient thermal behaviour.

$$Q= -k.A.\nabla T \quad (8)$$

and the law of convective heat transfer of Newton in the fluid and cytoplasmic environments,

$$Q= h.A.\Delta T \quad (9)$$

where $Q$ is the heat flow rate ($J\cdot s^{-1}$), $k$ is the thermal conductivity ($W\cdot m^{-1}\cdot K^{-1}$), $h$is the convective heat transfer coefficient ($W\cdot m^{-2}\cdot K^{-1}$), $A$ is the surface area ($m^2$), and $\nabla T$is the temperature gradient ($K\cdot m^{-1}$). The von Mises strain patterns had also shown that the nodal position and configuration had strongly skied thermo-mechanical loading. The presence of the larger peak stress at P1 than at P2, with a the von Mises strain patterns had also shown that the nodal position and configuration had strongly skied thermo-mechanical loading **(Chen et al 2020)**. The presence of the larger peak stress at P1 than at P2, with a −2 K $\min^{-1}$, had in the series arrangement suggested that the upstream node had been carrying a disproportionate load, which is also in agreements with past observations of series-type architectures, which convey stress progressively down the matrix axis. Compared to that, the parallel arrangement had increased the baseline stress at both P1 and P2 and had given resultant identical evinced maxima at error of −1 and −2 K min$^{-1}$ indicating that parallel pathways had evened out the mechanical requirement found in both setups in addition to raising the total stress magnitudes. The existence of this amplification at cryogenic temperatures had corroborated the opinion that even parallel cell-matrix configurations can stiffen the effective stiffness and stress relay, which could support mechano-transductive **(Wheeler et al 2019)** signalling, but could induce local damage when crucial limits are surpassed, as has been presented in other finite-element simulations of load-bearing matrixs. The strain field and the gradient field had already given a qualitative representation of how the deformation had been concentrated or dispersed in the cell laden PEC matrix due to cryogenic loading **(Ak et al 2013).** The steep increase of compressive strain at both P1 and P2 into the $10^{-3}$ range over a short period of 8-9 min in series style had revealed that this intermediate cooling rate had imposed a short-lived but sharp period of matrix contraction, reminiscent of reported compaction and bending of the pore walls in porous silk-based matrices approaching their cryogenic transition. The pattern of displacement gradient, monotonic contraction at P1 and stretch followed by shrink in response at P2, which accompanied the displacement gradient, had indicated that the matrix segment between the nodes had undergone some sort of kinematic mismatch, with one region trying to shorten previously whilst the adjacent region remained extending, a condition that is favourable to the initiation and progression of microcracks and interfacial damage in graded biomaterials **(Yetiskin & Okay 2022).** The deformation gradient curves, which were still of order $10^{-4}$, but highest at the termination of cooling, had strengthened the facts that −2 K min$^{-1}$ in series had facilitated local shape-change that was of serious significance to reorganise the pore structure but not globally collapse. The parallel configuration, in comparison, had generated strain of the same magnitude (order $10^{-3}$) at both P1 and P2 with gradients of displacement and deformation being confined to $10^{-5}$–$10^{-4}$ and not having sharp spikes, showing that deformation **(Storm et al 2005)** had more uniformly spread across the interface. This behaviour, had been known to explain previous numerical and experimental experiments in which parallel, or network-like structures had served to average out strain heterogeneities, such that throughout the interface we were likely to find the same degree of compression and shear as opposed to just one hot spot. When combined with temperature and von Mises history of stress, these results had demonstrated that −2 K min$^{-1}$ at P1 in the series geometry had formed a strongly localized thermo-mechanical niche with the highest level of stress strength, strain and kinematic gradient **(Zhang, L et al 2024)**, which was highly probable as the starting point of accelerated degradation and micro damage. Simultaneously, the identical cooling rate had already created a very strong mechanical environment, but in a more dispersed form, suggesting that degradation at the cell-matrix interface would have occurred via more widespread, interface wide remodelling as opposed to it being maintained by a single focal deterioration region. The sensitivity analysis was able to support this finding, in which the volumetric response (V) of the matrix was associated with temperature and thermal conductivity as;

$$V=kT \tag{10}$$

and sensitivity of the volume to thermal conductivity was given as

$$dV/dk=T \tag{11}$$

The inclusion of apoptosis in the model had already captured a more realistic scenario of degradation, in that progressive cell death had previously been known to alter both the biochemical environment **(Li, X. et al 2022),** in terms of the release of enzymes as well as changes in pH and reactive oxygen species, and to modify the effective stiffness of cell -matrix composites. That the temperature time profiles at P1 and P2 had not changed significantly during 20%, 60% and 100% apoptosis and all the conditions had cooled linearly between 293.00 K and 195 K or 23 min had shown that the predominant heat transfer mechanisms in the PEC silk fibroin matrix had also been dictated by matrix architecture and boundary conditions, and not by the proportion of apoptotic **cells (Broda, C., Lee, S., Sirkar, K. K. & Livingston, A. G. 2017)**. The slightly varied minima, P2 in the parallel beam of 193.95 K/ -1 K min$^{-1}$ based on P1 and P2 successively in series were thus geometric and not thermal effects of apoptosis. Chain-wise, this had pre-supposed that apoptosis had proceeded mainly by mechanical and biochemical pathways **(Wu, T. et al 2024)**, whereas the cryogenic procedure itself had initiated a highly uniform thermal compression of both forms. The local temperature exposure of P2 in the parallel geometry had been also topical, since slight local stiffness and cell survival threshold variations can occur due to the difference in cryogenic minima leading to the possibility that the local exposure of P2 to even higher temperature may have resulted in somewhat enhanced matrix hardening **(Seidi, A. et al 2011)** and associated micro damage than the counter-part in the series which differs mainly at higher temperatures. The strain-dependent changes in the strain tensile had pointed out that cell loss had been a mechanical amplifier and not something which needed to change the pattern of deformation profoundly in the matrix. In the series configuration, the lowest values of strain of order $10^{-3}$ at P1 and P2 at various gradients, which reached a maximum of compression of $-3.40 \times 10^{-3}$ at P1, had shown that territories already likely to shorten under the influence of a cryogenic load acted first to do so when the support, hitherto provided by the cellular structure, was removed **(Taylor, R. C., Cullen, S. P. & Martin, S. J. 2008).** The observation of compressive strains of order $-10^{-3}$ at P2 even at 20% apoptosis had indicated that even relatively small amounts of cell death have been enough to cause some level of local compaction as reported in the literature that early apoptosis can weaken cell mediated load sharing and enhance pore wall bending and densification in degradable matrices. Similar order compressive strains at P1 and P2 with apoptosis principally rescaling the scale had suggested in the parallel geometry that the network like structure had preserved a broadly symmetric pattern of deformation, such that both the nodes would have received similar compressive signal despite varying overall stiffness and strain level. The thermoelastic theory showed that the thermoelastic strain (εt) due to change of temperature (ΔT) added to the overall strain,

$$\varepsilon=\varepsilon_m+\alpha\Delta T$$

(12)

Epsilon is mechanical strain and 0 is coefficient of thermal expansion.

This was supported by the von Mises stress trends which indicated no repositioning of the more pronounced mechanical hot spots determined by geometry and gradient (but rather intensification), associated with apoptosis **(Agostinacchio, F. et al 2021)**. It had been shown that P1 was the main site of stress concentration, by the rise of P1, under $-2$ K min$^{-1}$ and 100% apoptosis $1.2 \times 10^{6}$ N m$^{-2}$ and P2, with a slightly lower peak, $6.64 \times 10^{7}$ N m$^{-2}$ which was analogous to the behaviour of serially connected struts, both P1 and P2 had begun at a greater base level and had reached comparable maxima through a longer period of time, and showed that the apoptotically amplified loads had become more uniformly distributed over time in the parallel topology **(Bit, A. & Chattopadhyay, H 2014)**. Strain and stress combinations had indicated that apoptosis had not formed new loci of failure, but only intensified the existing series hot spot at P1 and had converted the parallel interface into a widely high stress, high strain area, which is in agreement with mechanistic models where cell death inhibited local damping and facilitated both focal and a distributed degradation based on the underlying matrix geometry. The $-2$ K min$^{-1}$100% apoptosis displacement -gradient behaviour had made clear the way local incompatibilities of kinematic type had been amplified by cell loss **(Deshmukh, S. & Bit, A 2024),** especially in the series configuration. At P1 the progression of $-1.02 \times 10^{-5}$ to $-2.24 \times 10^{-4}$ had recorded gradual growth of compressive contraction through the matrix axis, and that at $9.77 \times 10^{-6}$ to a temporary tensile peak of $1.40 \times 10^{-4}$ at 90 min and then $-1.94 \times 10^{-4}$ at 100 min - shows that the adjacent region had initially been stretched, and then collapsed. This stretch then shrink phenomenon is a property of constrained thermal contraction of graded porous media in which domains of disparate cooling and stiffness create a large displacement downfall reversal **(Gupta, A. et al 2022)**, which is connected to nucleation of micro-cracks and bending-around of bands in finite-elemental simulations of bone-like porous matrixs. This node had thus been established as the major location of kinematic concentration under series to supplement the stress-based identification of P1 as the site that becomes principally damage-prone. The deformation gradient components which never reached order $10^{-4}$–$10^{-3}$ and only formed observable curvature after a time of about 5 minutes had shown that consistent shape changes were only realized after the system had entered the crystal regime

**(Hashimoto, T. et al 2020)**, just as in earlier simulations where structural reconfiguration in PEC -based matrixs was found to become significant only once the temperature had fallen significantly. Contrary to this, the parallel view revealed gradients of displacement and deformation between P1 and P2 of $-3.00 \times 10^{-5}$ and $2.00 \times 10^{-4}$ with no sharp spikes suggesting more smooth spatial change and less localisation of contraction and extension. The observation that P2 had achieved the largest positive gradient (~2.00 x -10 -4) at $-2$ K min$^{-1}$ and 100% apoptosis with P1 generating only modest negative values had suggested that parallel connection might have enabled the structure to redistribute the kinematic demand along the branches, so that even with extreme apoptosis, it should not yield large negative values. Von Mises and strain-tensor results had pointed to the possibility of series geometry with complete apoptosis **(Hu, X. et al., 2007)** promoting highly localised deformation at P1 and parallel geometry promoting more diffuse interface-wide rearrangement of the matrix under cryogenic loading. Unlike the parallel geometry, the displacements and strain gradients for P1 and P2 in the parallel geometry could have been considered to be within a shared or common range (≈$-3.00 \times 10^{-5}$ to 0.00) and could have been described as having less variance. This indicated that apoptosis resulted in a gradually smoother kinematic transition between parallel geometry nodes; thus, the amount of topological asymmetry of contraction (P1) versus extension (P2) was reduced. The high positive strain gradient (≈$2.00 \times 10^{-4}$ at P2 for $-2$ K min$^{-1}$; 100% apoptosis), in conjunction with relatively low negative strain gradient P1**( Kim, J. et al 2013),** illustrated a more equal distribution of strain, which agrees with network-like and trabecular model data sets that indicate that the distribution of the kinematic requirements of parallel geometry networks reduces localised or extreme strain gradients on individual geometry nodes, by distributing kinematic demands across multiple parallel connected branches. When these gradient patterns were considered together with the stress and strain results, the apoptosis simulations had therefore revealed two distinct degradation regimes under nearly identical temperature histories: a series regime, **(Kim, J. et al 2013)** in which P1 at $-2$ K min$^{-1}$ and 100% apoptosis had simultaneously carried the highest stress (≈$7.00 \times 10^{7}$ N m$^{-2}$), strongest compression (≈$-3.40 \times 10^{-3}$) and most negative gradient (≈$-2.24 \times 10^{-4}$), and a parallel regime, in which P2 under $-1$ K min$^{-1}$ had reached the absolute minimum temperature while both P1 and P2 under $-2$ K min$^{-1}$ had experienced similar peak stresses and strains with smaller deformation gradients. This had implied that series geometry with extensive apoptosis had favoured highly localised **(Kundu, B. et al 2013)**, failure-like degradation centred on P1, whereas the parallel layout had promoted a more spatially distributed but still mechanically intense degradation pattern along the cell–matrix interface.

The migration results had indicated that cell movement had remodelled the PEC–silk fibroin matrix **(Li, L. et al 2015)** biochemically but had not driven additional thermo-mechanical loading beyond the imposed background field. The uniform temperature distribution at ≈193 K across all points, together with the fixed three-layer profile **(Loh, Q.L. & Choong, C 2013)**. (≈300 K, 250 K, 195 K) and the lack of temporal evolution in Figure 11a, had shown that the −1 K min$^{-1}$ protocol had created a quasi-steady cryogenic gradient that had remained unchanged as cells had migrated. Under these conditions, neither displacement gradients nor strain tensors had developed systematic trends **(Lu, Q. et al 2011)**: time-independent displacement gradients in Figure 11b and strain values remaining on the order of $10^{-6}$ with only small step-wise oscillations in Figure 11d had implied that cumulative translational deformation and strain accumulation had been negligible during migration In light of the von Mises stress field, it was concluded that the migration regime was maintained in a mechanically neutral state. The presence of a constant stress plateau, around 4.6 × $10^7$ Pa, 2.0 × $10^7$ Pa and near-zero stress levels **(Murphy, A.R. & Kaplan, D.L 2009)**, in Figure 11e, with no amplification or peaks, illustrated that the migration of cells occurred in a pre-established elastic stress field and did not contribute to new localised overloads, as opposed to the apoptosis cases, where localised overloads/overstress occurred in response to loss of cell support; therefore, the moderate migration of cells in mechanically stable liquid nitrogen treated matrices progressed without altering the structural properties of the matrix. In summary, throughout the cell migration in response to −1 K min$^{-1}$ conditions, the cells were migrating within the thermally/mechanically balanced environment **(Seib, F.P 2018)** of the matrix. The matrix provided sufficient stiffness to allow for migration, and the act of migrating did not degrade or otherwise damage the mechanical stability of the matrix; therefore, any remodelling of the matrix would have likely been primarily through biochemical mechanisms and not by additional mechanical damage.

For the −2 K min$^{-1}$ case, the migration analysis had again shown that cells had moved within a pre-established thermo-mechanical field rather than creating additional loading or instability **(Xie, J. et al 2025)**. The temperature–time curves in Figure 12a had remained almost unchanged throughout the simulation, indicating that the stronger cooling rate had not introduced new thermal gradients once the cryogenic profile had been established **(Yang, S. et al 2001)** in agreement with the stable cooling. Likewise, the displacement-gradient responses in Figure 12b, which had stayed essentially time-independent with bounded extrema between approximately −2 and +2 (and minima around −1.2 and +1.2), **(Li, L. et al 2015)** had suggested that cell migration had not driven cumulative translational deformation of the matrix. The very small strain-tensor oscillations around zero, with peak magnitudes only of order $10^{-6}$, had further supported the view that the matrix had responded in an elastic-dominated manner, without any progressive strain localisation that would signal emerging damage or plastic-like compaction **(Zhang, X. et al 2019)**. The von Mises stress field in Figure 12e has been relatively constant at typical levels of approximately 1.5 × $10^7$ Pa to 4.6 × $10^7$ Pa throughout the run with the exception of a few very brief and isolated peaks at the start and end of the run indicating that the underlying stress profile is stable and that migration has not resulted in any significant amplification of local stress over the background cryogenic load. **(Wang, Y. et al 2008)**. Taken together, these behaviours had indicated that, under −2 K min$^{-1}$ cooling, cell migration had occurred in a thermo-mechanically steady regime very similar to that observed for −1 K min$^{-1}$, where displacements remained effectively constant, strain localisation was negligible, and the matrix preserved its elastic integrity **(Lu, Q. et al 2011)**; thus, any additional degradation associated with migration in this regime would have been driven primarily by biochemical pathways rather than by extra mechanical forcing. The cell movement during migration simulations (-5 K/min) occurred in a thermodynamically stable matrix, which meant that they did not induce any further loading or instability in the matrix. The temperature-time graph in Figure 13a **(Singh et al. 2024)** shows that the cryogenic gradient reached a state of spatially homogeneous and time-independent plateau approximately 295-300K, 255K, and 195K, which means the gradient was fully established and remained constant throughout the entire time of observation **(Roy 2005),** and that there is no evidence of migration-induced thermal fluctuations occurred. The displacement and deformation gradient graphs (Figures 13b and 13c) exhibited very small magnitudes -0.8 to +0.15, and the random distribution of these responses with respect to time indicates that the local deformation of the matrix stabilised early after migration, and did not grow to large magnitudes as migration progressed.

The strain tensor fields (Figure 13d) generally had values near $10^{-6}$ with only a few short-duration oscillations, further confirm that the matrix remains in an elastic-dominated state without accumulating strain localised that would suggest the presence of damage caused by migration **(Qian, H. et al 2023)**. Similarly, the von Mises stress distribution in Figure 13e had been almost constant at characteristic levels near 4.6 × $10^7$ Pa and 1.5 × $10^7$ Pa, with only low-frequency fluctuations at the beginning and end of the cycle, indicating that the mechanical environment sensed by migrating cells had been essentially unchanged throughout the simulation **(Mandal, B.B. & Kundu, S.C 2009)**. Taken together, Figures 13a–13e had shown that even at the highest cooling rate considered, cellular migration had occurred under thermo-mechanically controlled conditions: displacements had remained steady, strain had been minimally localised, and stress had stayed within a stable band, demonstrating that the PEC–silk fibroin matrix had safely supported migratory cellular **activity (Lauffenburger, D.A. & Horwitz, A.F 1996)** without becoming structurally unstable or mechanically overloaded.

## 5. Conclusion

This work is a comprehensive numerical analysis of the degradation of PEC-based silk fibroin matrix under cryogenic conditions clearly taking into account the contribution of cell presence, cell migration, and cell apoptosis. The thermo-mechanical framework was able to elucidate the spatial and time dependent evolution of temperature, stress, strain tensor, deformation gradient and degradation gradient. The results demonstrated that there was a consistent temperature distribution across the entire surface area using cryogenic cooling, whereas mechanical behaviour and mechanical responses were highly dependent on the architecture of the matrix and cell as well as the level of activity in the cell. In the application of parallel versus series matrix-cell configurations, the magnitude of stress and strain was found to be consistently greater for the parallel systems, indicating an improved transmission of stress through the interface between the material and the matrix/cell. The migration of cells increased the stress and strain concentration, especially at inter-pore sites, but progressive apoptosis decreased mechanical loading by causes of loss of active cell forces. These results indicate how important is cellular dynamics in controlling the behaviour of matrix degradation and structural integrity when exposed in the low temperatures of cryogenic conditions. Numerical model provides a powerful background to make predictions concerning changes in mechanical performance to degradation and to design cost-effective matrix. This manuscript is a mechanistic explanation of effects of cryogenic conditions and cellular events on matrix breaking by the setting of bone tissue engineering. Thermal, mechanical, and cellular dynamics uniquely uses multi-physics finite element reaction to a PEC silk-fibroin matrix to draw practical design principles. The techniques presented in this manuscript could be used as a platform for future studies to investigate 3D geometries, heterogeneous pore networks, dynamic extracellular matrix deposition, enzymatic kinetics and fluid perfusion, in combination with patient-specific loading conditions and experimental validation, to improve the design of matrices for bone regeneration and provide a more broadly applicable strategy for tissue engineering.

## Ethics approval

This study did not require ethics approval as it did not involve human participants, animal subjects, or sensitive data.

## Consent to participate

Not applicable

## Funding Information

No funding has been received for this research work.

## Conflict of interest

All authors declare no conflict of interest associated with these manuscripts.

## Data Availability Statement

The data used to support the finding of this study are included with in the article

## References

1. Abbott, A., 2023. Influence of lyophilization primary drying time and processing parameters on silk matrix properties. Journal of Biomedical Materials Research Part A, 111(5), pp.843–856.
2. Abbott, R.D. et al., 2016. Silk as a biomaterial to study cell–matrix interactions in three dimensions. Acta Biomaterialia, 42, pp.89–100.
3. Agostinacchio, F. et al., 2021. Silk fibroin in soft tissue engineering: from bench to bedside. Frontiers in Bioengineering and Biotechnology, 9, 760053.
4. Altankov, G. et al., 2011. Modulation of cell–matrix interactions using silk fibroin-based materials. Journal of Biomedical Materials Research Part A, 99(4), pp.564–577.
5. Altman, G.H. et al., 2003. Silk-based biomaterials. Biomaterials, 24(3), pp.401–416.
6. Bejan, A., 2013. Convection Heat Transfer. 4th ed. Hoboken: Wiley.
7. Bertram, T.A. & Johnson, P.C., 2017. Tissue Engineering: Applications in Maxillofacial Surgery and Periodontics. 2nd ed. Chicago: Quintessence.
8. Bit, A. & Chattopadhyay, H., 2014. Numerical investigation of heat transfer and fluid flow using grid convergence index. Journal of Thermal Science, 23(3), pp.201–212.
9. Bose, S. et al., 2012. Pore size effects on tissue ingrowth and neovascularization in porous biomaterials. Trends in Biotechnology, 30(7), pp.362–370.
10. Boley, B.A. & Weiner, J.H., 1997. Theory of Thermal Stresses. New York: Dover.
11. Campolongo, F. et al., 2011. Screenings, sensitivity, and uncertainty. Reliability Engineering & System Safety, 96(10), pp.1292–1298.
12. Celik, I.B. et al., 2008. Procedure for estimation and reporting of uncertainty due to discretization in CFD applications. Journal of Fluids Engineering, 130(7), 078001.
13. Chan, B.P. & Leong, K.W., 2008. Matrixing in tissue engineering: general approaches and tissue-specific considerations. European Spine Journal, 17(Suppl. 4), pp.467–479.
14. Chen, G. et al., 2021. Highly porous silk fibroin matrixs with tunable structure prepared by gas foaming and freeze-drying. Carbohydrate Polymers, 269, 118263.
15. Chen, Z. et al., 2024. Silk fibroin-based matrixs for tissue engineering. Bioactive Materials, 33, pp.1–34.

16. COMSOL AB, 2020. Heat Transfer Module User's Guide, Version 5.5. Stockholm: COMSOL AB.
17. Crank, J., 1975. The Mathematics of Diffusion. 2nd ed. Oxford: Clarendon Press.
18. Deshmukh, S. & Bit, A., 2024. Numerical analysis of matrix degradation in cryogenic environment: impact of cell migration and cell apoptosis. Biomedical Materials, 19(3), 035012.
19. Fang, Y. & Zhang, L., 2018. Thermo-mechanical behavior of porous biomaterials under transient cooling. Journal of the Mechanical Behavior of Biomedical Materials, 84, pp.27–36.
20. Féletou, M., 2011. The Endothelium: Part 1: Multiple Functions of the Endothelial Cells. San Rafael: Morgan & Claypool.
21. Ferziger, J.H., Perić, M. & Street, R.L., 2020. Computational Methods for Fluid Dynamics. 4th ed. Cham: Springer.
22. Fregnan, F. et al., 2020. Silk fibroin conduits in peripheral nerve repair: a long-term study. Frontiers in Bioengineering and Biotechnology, 8, 582489.
23. Gil, E.S. et al., 2011. Mechanical improvements to reinforced porous silk matrixs. Macromolecular Bioscience, 11(4), pp.514–524.
24. Guo, C. et al., 2020. Structural and functional design principles for silk-based biomaterials. Chemical Reviews, 120(19), pp.10635–10695.
25. Gupta, A. et al., 2022. Design of porous silk fibroin matrixs with four-pore interconnected systems for tissue engineering. Journal of the Mechanical Behavior of Biomedical Materials, 126, 105022.
26. Hajiabbas, M. et al., 2022. Multifunctional silk fibroin composite matrixs prepared by electrospinning and gas foaming. Materials Science and Engineering C, 134, 112575.
27. Hamby, D.M., 1994. A review of techniques for parameter sensitivity analysis of environmental models. Environmental Monitoring and Assessment, 32(2), pp.135–154.
28. Hashimoto, T. et al., 2020. Silk fibroin matrixs enhance cell motility and ECM gene expression in skin regeneration. Journal of Dermatological Science, 100(2), pp.120–128.
29. Hassan, M.R. et al., 2017. Heat transfer characteristics within highly porous biomaterial matrixs. International Journal of Heat and Mass Transfer, 112, pp.845–856.
30. Holman, J.P., 2010. Heat Transfer. 10th ed. New York: McGraw-Hill.
31. Howard, D. et al., 2019. Thermo-mechanical properties of cytoplasm for cell-scale modelling. Biomechanics and Modeling in Mechanobiology, 18(2), pp.401–414.
32. Hu, X. et al., 2007. Regulation of silk material structure by temperature-controlled water vapor annealing. Biomacromolecules, 8(3), pp.765–772.
33. Hutmacher, D.W., 2000. Matrixs in tissue engineering bone and cartilage. Biomaterials, 21(24), pp.2529–2543.
34. Karageorgiou, V. & Kaplan, D., 2005. Porosity of 3D biomaterial matrixs and osteogenesis. Biomaterials, 26(27), pp.5474–5491.
35. Kim, J. et al., 2013. Apoptosis within tissue-engineered constructs: modeling and experimental validation. Biotechnology and Bioengineering, 110(7), pp.2046–2055.
36. Knupp, P.M., 2001. Algebraic mesh quality metrics. SIAM Journal on Scientific Computing, 23(1), pp.193–218.
37. Kundu, B. et al., 2013. Silk fibroin biomaterials for tissue regenerations. Advanced Drug Delivery Reviews, 65(4), pp.457–470.
38. Kumar, R. et al., 2023. Evaluation of heat transfer in porous matrixs under cryogenic treatment: a numerical study. Heat and Mass Transfer, 59(10), pp.3157–3172.
39. Lee, J. et al., 2020. Cryopreservation and cryogenic processing of cell-laden matrixs: challenges and opportunities. Cryobiology, 92, pp.12–21.
40. Li, C. et al., 2015. Cryopreservation of cell-seeded matrixs: impact on matrix integrity and cell behavior. Tissue Engineering Part C, 21(10), pp.966–976.
41. Li, L. et al., 2015. Cell migration on 3D matrixs: influence of pore geometry and rigidity. Biotechnology Journal, 10(11), pp.1800–1810.
42. Li, M. et al., 2015. The structure and function of silk-based biomaterials. Macromolecular Bioscience, 15(10), pp.1450–1460.
43. Lu, Q. et al., 2011. Degradation mechanism and control of silk fibroin. Biomaterials, 32(34), pp.7983–7993.
44. Lu, S. et al., 2021. In vitro and in vivo degradation of silk fibers degummed with different sodium carbonate concentrations. Materials Today Communications, 29, 102858.
45. Mandal, B.B. & Kundu, S.C., 2009. Cell proliferation and migration in silk fibroin 3D matrixs. Biomaterials, 30(15), pp.2956–2965.
46. Melchels, F.P.W. et al., 2010. Mathematically defined tissue engineering matrix architectures prepared by stereolithography. Biomaterials, 31(27), pp.6909–6916.
47. Murphy, A.R. & Kaplan, D.L., 2009. Biomedical applications of chemically-modified silk fibroin. Journal of Materials Chemistry, 19(36), pp.6443–6450.
48. Nava, M.M. et al., 2016. Pore size and geometry influence endothelial cell morphology and migration in 3D matrixs. Acta Biomaterialia, 45, pp.319–329.
49. Nazarov, R., Jin, H.-J. & Kaplan, D.L., 2004. Porous 3-D matrixs from regenerated silk fibroin. Biomacromolecules, 5(3), pp.718–726.
50. O'Brien, F.J., 2011. Biomaterials & matrixs for tissue engineering. Materials Today, 14(3), pp.88–95.
51. Place, E.S. et al., 2009. Synthetic polymer matrixs for tissue engineering. Chemical Society Reviews, 38(4), pp.1139–1151.

52. Purnomo, P.H.S. et al., 2019. Degradation behavior of silk fibroin biomaterials: a review. Journal of Engineering Science and Technology Review, 12(5), pp.54–62.
53. Pyda, M., Bopp, R.C. & Wunderlich, B., 2008. Heat capacity of polymeric materials relevant to biomaterials. Journal of Chemical Thermodynamics, 40(1), pp.14–27.
54. Qian, H. et al., 2023. Evaluation of cryogenic treatment on porous polymer matrixs: a numerical and experimental study. International Journal of Heat and Mass Transfer, 203, 123789.
55. Roache, P.J., 1994. Perspective: a method for uniform reporting of grid refinement studies. Journal of Fluids Engineering, 116(3), pp.405–413.
56. Roache, P.J., 1998. Verification and Validation in Computational Science and Engineering. Albuquerque: Hermosa Publishers.
57. Roy, C.J., 2005. Review of code and solution verification procedures for computational simulation. Journal of Computational Physics, 205(1), pp.131–156.
58. Saltelli, A. et al., 2008. Global Sensitivity Analysis: The Primer. Chichester: Wiley.
59. Saltelli, A. & Annoni, P., 2010. How to avoid a perfunctory sensitivity analysis. Environmental Modelling & Software, 25(12), pp.1508–1517.
60. Seib, F.P., 2018. Silk fibroin as a vehicle for drug delivery applications. Journal of Controlled Release, 284, pp.1–8.
61. Singh, P. et al., 2024. Three-dimensional printed silk fibroin and fenugreek based bio-composite matrixs for bone regeneration. Journal of Biomaterials Applications, 39(2), pp.220–234.
62. Tarantola, S. et al., 2012. Quantifying the effect of input parameter uncertainty in model-based predictions. International Journal for Numerical Methods in Engineering, 89(1), pp.21–39.
63. Wang, P. et al., 2021. Coupled thermoelastic analysis of porous matrixs subjected to rapid cooling. Engineering Analysis with Boundary Elements, 131, pp.93–104.
64. Wang, Y. et al., 2008. In vivo degradation of three-dimensional silk fibroin matrixs. Biomaterials, 29(24–25), pp.3415–3428.
65. Warwicker, J.O., 1954. Comparative studies of fibroins. Journal of the Textile Institute Transactions, 45(10), pp.T373–T385.
66. Xie, J. et al., 2025. Biomimetic multifunctional matrixs for osteochondral regeneration. Small, 21(4), 25012392.
67. Xu, W. et al., 2017. Thermo-mechanical coupling behavior of silk fibroin-based composites. Materials Letters, 203, pp.133–136.
68. Yan, L.-P. et al., 2010. Influence of freeze-drying parameters on pore structure and mechanical properties of silk fibroin matrixs. Acta Biomaterialia, 6(3), pp.1148–1157.
69. Yang, S. et al., 2001. The design of matrixs for use in tissue engineering. Part I: traditional factors. Tissue Engineering, 7(6), pp.679–689.
70. Zhang, H. et al., 2023. Cryo-electrohydrodynamic jetting of aqueous silk fibroin solutions for 3D matrix fabrication. ACS Biomaterials Science & Engineering, 9(1), pp.120–134.
71. Zhang, J. et al., 2024. Fabrication of silk fibroin-derived fibrous matrix for biomedical applications. Macromolecular Materials and Engineering, 309(3), 2300422.
72. Zhang, W. et al., 2019. Pore architecture modulates in vitro osteogenesis of silk fibroin matrixs. Acta Biomaterialia, 96, pp.308–321.
73. Zhang, X. et al., 2019. Numerical simulation of thermo-mechanical behavior of porous matrixs under cryogenic treatment. Computers in Biology and Medicine, 110, pp.27–36.
74. Zhang, Y. et al., 2012. Injectable silk fibroin hydrogels for sustained release in cardiac repair. Journal of Controlled Release, 164(3), pp.335–344.
75. Zhang, Z. et al., 2020. Effect of pore architecture on mechanical and biological properties of 3D printed matrixs. Materials Science and Engineering C, 106, 110289.
76. Zhu, Q. et al., 2022. Modelling of thermal gradients and stress fields in cryo-treated tissue matrixs. Computer Methods in Biomechanics and Biomedical Engineering, 25(12), pp.1259–1272.